The Low-Lying Excited States of Pyridine

Zheng-Li Cai and Jeffrey R. Reimers*

School of Chemistry, University of Sydney, NSW 2006, Australia

Received: March 14, 2000; In Final Form: June 6, 2000

We assign the observed phosphorescence and high-resolution singlet-to-triplet absorption spectra of pyridine, performing large model vibronic coupling calculations involving six active modes and three near-degenerate electronic states, $^3A_1$, $(2)^3A_1$, and $^3B_1$. Vibronic coupling primarily through ν_{8a} between $^3A_1$ and $(2)^3A_1$ results in the breakdown of the pseudo-parity selection rule: the lower surface has a double minimum, with each well corresponding to a diabatic single-determinant (π,π^*) excitation. These states then strongly vibronically couple to $^3B_1$ primarily through ν_{16b}, resulting in a very complex $^3A'$ manifold. In addition, for the singlet manifold, we detail a low-lying conical intersection between $^1B_1$ and $^1A_2$ and suggest that this intersection should have observable consequences for excited-state dynamics. These conclusions are obtained through the examination of all states below 5 eV in energy [$^1B_1$ (S_1), $^1B_2$ (S_2), $^1A_2$ (S_3), $^3A_1$, $(2)^3A_1$, $^3B_1$, $^3A_2$, and $^3B_2$], performing CIS, CASSCF, CASPT2, CCSD, CCSD(T), EOM-CCSD, CNDO/S, B3LYP, BLYP, TD-B3LYP, and TD-BLYP calculations for the vertical excitation and emission energies; equilibrium, transition-state, and conical-intersection structures; vibration frequencies; spin−orbit couplings; vibronic couplings; ESR atomic spin densities; and low-resolution absorption and emission band contours. Special techniques are developed for the application of the electronic structure methods to the evaluation of the required molecular properties, and it is shown that the application of a wide range of methods is required both because of the diversity of the required properties and because the intrinsic errors in the methods are of magnitudes that are chemically significant.

1. Introduction

Pyridine, the simplest aza-aromatic molecule, has been extensively studied with regard to the photophysics and photochemistry of its low-lying excited states. Although it is often thought of as a paradigm molecule, its properties are actually somewhat unusual, and many features of the lowest few triplet and singlet excited states remain to be determined. An excellent summary of the state of knowledge in this area can be found in the review of Innes, Ross, and Moomaw[1] and in the very recent work of Chachisvilis and Zewail.[2] Much is known and understood about the singlet manifold, whereas much is known but little is understood about the triplet states. Fortunately, the ground (X $^1A_1$) state has been well-characterized by various high-resolution spectroscopic[1,3−7] and computational[8−11] methods, and this work forms a framework for consideration of the properties of the excited states.

Within the singlet manifold, the first excited state (S_1) is of $^1B_1$ symmetry and (n,π^*) type. The band origin and a variety of vibration frequencies have been determined through high-resolution absorption,[3,12−14] fluorescence,[2,15−19] electron energy loss,[20] and optothermal[9] spectroscopy, but the absorption spectrum is weak and significantly obscured by the close-lying second excited state, $^1B_2$ (π,π^*). In 1972, Jesson et al.[21] deduced from the observed vibrational spacings in the out-of-plane "boat" vibrational mode ν_{16b} that $^1B_1$ (n,π^*) is quasi-planar with a double-well potential depth of 4 cm^{-1}. In 1997, Becucci et al.[9] studied this state using both high-resolution optothermal spectroscopy and complete-active-space self-consistent-field (CASSCF) calculations. Rotational analysis of their spectroscopic results revealed that this state is, on average, planar on the rotational time scale, and the CASSCF calculations also predicted a planar structure. On the other hand, the very recent femtosecond dynamical studies of Chachisvilis and Zewail[2] are suggestive of nonplanarity, this conclusion being supported by configuration-interaction-singles (CIS) geometry optimizations and time-dependent density-functional (TD-DFT) single-point energies. Neither set of calculations is authoritative, however, as it had not been demonstrated that the CASSCF potential-energy surface used was continuous with respect to displacements in ν_{16b}, CASSCF and CIS are low-level methods that do not include the effects of dynamic electron correlation, and TD-DFT geometry optimizations were not performed. We perform a variety of high-level ab initio and density-functional calculations and present a model for the structure of $^1B_1$ (n,π^*) that is consistent with all available experimental information. Also, it remains unclear whether the excited (π,π^*) states such as $^1B_2$, $^3B_2$, and $^3A_1$ retain C_{2v} symmetry. CASSCF calculations[2] again suggest high symmetry for $^1B_2$ (S_2), but we investigate the structure of all of these states in detail.

A property of the singlet manifold that may be important to excited-state dynamics but has not been explored is the rather low adiabatic energy of $^1A_2$ (S_3), a feature first noticed by Lorentzon, Fülscher, and Roos.[8] We explore this in detail, isolating a low-lying point of conical intersection between $^1A_2$ and $^1B_1$.

For the triplet manifold, much experimental information is available from low-resolution solution[22] and high-resolution gas-phase[23] singlet-to-triplet absorption spectroscopy, gas-phase phosphorescence spectroscopy,[24] electron spin−echo spectros-

* Author to whom correspondence should be addressed. E-mail: reimers@chem.usyd.edu.au.

10.1021/jp000962s CCC: $19.00
Published on Web 08/18/2000

copy in benzene crystal,[25−27] transient absorption spectroscopy,[28] and electron energy loss spectroscopy.[20,29] The high-resolution absorption spectra show only a few clumped lines with very unusual spacings; the spectrum beyond 2000 cm^{-1} above the first line is obscured by hot bands of the far more intense transitions to the singlet states. None of the observed lines has been assigned, but the spectrum is interpreted[23] as arising from two separate electronic transitions, and a variety of postulates have been made concerning their identity. Theoretical calculations (see, e.g., refs 8, 20, and 30−34) have shown that both $^3A_1$ (π,π^*) and $^3B_1$ (n,π^*) are the most likely candidates. At some geometry, these two states will form a conical intersection,[35] and Selco, Holt, and Weisman[28] evoked this mechanism to explain their observed transient absorption kinetics: the lower-lying electronic state will attain a double-minimum potential along a vibrational coordinate identified to be ν_{16b} (the ring boat deformation), producing a nonplanar structure. As computation had predicted that, at vertical excitation, the $^3A_1$ (π,π^*) state is lowest in energy (a result supported by most subsequent calculations[8,20,31,34]), they reasoned that it is this state that becomes nonplanar. The observed phosphorescence spectrum[24] is very broad and unstructured, implying[1] a large distortion in a low-frequency mode, but no assignment of this spectrum has been established. Electron spin−echo studies[25−27] in benzene crystal show that the equilibrium structure is indeed distorted along ν_{16b}, the zero-point vibrational level being interpreted as comprising 80% $^3A_1$ (π,π^*) character and 20% $^3B_1$ (n,π^*) character. However, subsequent calculations[32,33] of the structure of these two electronic states suggested that the lower, distorted state is in fact $^3B_1$ (n,π^*); alternatively, CIS calculations,[34] which do not allow for dynamic electron correlation, predict that *both* states have C_{2v} symmetry. In this study, we provide assignments for all of the observed spectra, including the key vibronic transitions contributing to the high-resolution absorption spectra.

A large number of computational studies have been performed on the excited states of pyridine. The most recent include the 1988 (SAC-CI) study of Kitao and Nakatsuji;[31] Walker et al.'s[20] 1989 and Buma et al.'s[33] 1989 multireference doubles configuration-interaction (MRDCI) studies; Nagaoka and Nagashima's[32] 1990 unrestricted Hartree−Fock (UHF) and unrestricted Møller−Plesset perturbation-theory (UMP2) calculations; Forsman et al.'s[34] 1992 CIS study; Roos et al.'s[8,36] 1992 and 1995 complete-active-space self-consistent-field (CASSCF) with second-order perturbation-theory correction (CASPT2) studies; Del Bene et al.'s[37] 1997 equation-of-motion coupled-cluster (EOM-CCSD) with corrections for triples excitations [EOM-CCSD-(T)] study; Nooijen and Bartlett's[38] related similarity-transformed equation-of-motion coupled-cluster (STEOM-CCSD) study; Becucci et al.'s[9] 1997 CASSCF study; Bauernschmitt and Ahlrichs' 1996 time-dependent density-functional (TD-DFT) study;[39] and finally Chachisvilis and Zewail's 1999 CASSCF, CIS, and TD-DFT study[2] of S_1 and S_2 surfaces and the isomerization of S_2 to a very low energy prefulvene form. Our study is most similar to this later one in that we are concerned with the shapes of the potential-energy surfaces, their intersections, and the interpretation of spectroscopic data, and we also apply a range of computational methods. However, we consider different molecular properties, concentrating on the S_1-S_3 conical intersection (section 3.3.2), the nature of the triplet manifold (Sections 2 and 3.4.1), and the excitation energies (section 3.2), the equilibrium structures (sections 3.3 and 3.4), vibrational motions (section 3.5), and electronic absorption and emission spectra (section 4) of all of the pyridine-like excited states.

Specifically, in this paper we study the ground state (S_0), the $^1B_1$ (S_1), $^1B_2$ (S_2), and $^1A_2$ (S_3) singlet excited states, as well as the $^3A_1$, $(2)^3A_1$, $^3B_1$, $^3A_2$, and $^3B_2$ triplet excited states of pyridine, determining the absorption and emission vertical excitation and emission energies, the equilibrium structures, the normal modes of vibration (sometimes corrected for diagonal anharmonicity), spin densities, spin−orbit coupling constants, and vibronic coupling constants, using these results to simulate the observed spectra through large vibronic coupling calculations. These excited states are selected as they are the only states that could conceivably contribute to the lowest-energy singlet and triplet excited-state manifolds. The computational methods used are CASSCF,[40] CASPT2,[41] CCSD,[42] CCSD(T),[43] EOM-CCSD,[44] TD-DFT[39,45−48] using the B3LYP[49] and BLYP[50,51] functionals (TD-B3LYP and TD-BLYP) as well as direct DFT calculations using these same functionals, CIS,[34] and CNDO/S-CI.[52] The implementations used for these methods are described in Appendix A.1, while details of the CASSCF active space and its design criteria are discussed in Appendix A.2. These CASSCF calculations have significant problems associated with the continuity of the potential-energy surfaces, an effect that is often not properly considered (see, e.g., ref 9), and this issue is addressed in Appendix A.3.

We find that, to solve a problem with manifold complexity such as the nature of the lowest triplet hypersurface of pyridine, the use of a large range of electronic structure methods is essentials. Not every method can be applied to calculate all of the various data types required, and not every method is suitable for all applications. Also, the errors associated with the approximations used are small enough that, collectively, the actual scenario can be realistically described but large enough to cause significant perturbations to the shapes of nearly degenerate potential-energy surfaces. In Appendix A.4, the electronic structure methods are categorized into three types (multireference, single-reference, and ground-state-based), and the relative strengths and weaknesses are described. It is important to choose a method of the appropriate type, but one must be mindful of the varying level of accuracy that can be expected, estimating the accuracy of computed properties such as surface curvatures, conical intersection points, vibronic and spin−orbit couplings, etc., in a holistic way for each individual method.

In particular, we find that none of the commonly used methods (e.g., CASSCF, CIS, CNDO/S) used to calculate vibronic coupling constants are sufficiently accurate for our purposes. Hence, we introduce in section 4.2.2 a novel technique for their evaluation, in the strong-coupling limit, through analysis of the fully relaxed optimized geometries of the states. This approach is applicable using any electronic structure method, and here we use EOM-CCSD, a method that is much more accurate than the usual methods used to evaluate vibronic coupling constants.

A key aspect of this paper is the unification of a large number of different experimental observations on pyridine and the conclusions drawn from them. Previously, seemingly disparate conclusions have been drawn, but we show that often the differences are associated with subtleties of the representations of the excited states being used. Hence, we start by describing the various labels used to describe excited states (Born−Oppenheimer adiabatic, crude-adiabatic, and diabatic) in detail in section 2, along with subtleties in the use of symmetry labels. The primary nature of the transitions studied, expressed in terms

of molecular-orbital excitation, is discussed here, as is the pseudo-parity selection rule[53] that provides the basic model for (π,π*) electronic spectroscopy.

In section 3, we consider results obtained by electronic structure computation: vertical excitation energies, state assignments, relaxation within C_{2v} symmetry, full geometry relaxation, and excited-state vibration frequencies. A novel part of the vertical excitation energy analysis is that we deduce experimental values by re-analyzing, in section 3.2.1, the original spectra in order to obtain the average transition energy, not simply approximating this value using the energy of maximum absorption, and we also explicitly treat the zero-point energy correction. These affects, which are seldom considered, are shown to be larger than the errors associated with modern computational methods, and hence, their treatment is essential.

In section 4, we directly simulate the observed spectra, at the simplest level using the Franck−Condon harmonic oscillator analysis (with full treatment of Duschinsky rotation), but optionally considering also non-Condon effects, and, for the triplet manifold, using large-scale vibronic-coupling calculations.

2. The Nature of the Excited States Considered

The excited states with which we are concerned are the $^1B_1$, $^3B_1$, $^1A_2$, and $^3A_2$ (n,π*) states and the $^1B_2$, $^3B_2$, $^3A_1$, and $(2)^3A_1$ (π,π*) states. Unfortunately, a variety of different interpretations are possible for the meaning of these labels, each with its own realm of appropriateness. As the distinction between these interpretations is important, we consider them explicitly before describing our results in detail. Typically, we use these labels to indicate Born−Oppenheimer adiabatic states, states whose electronic nature changes continuously with the nuclear coordinates. Most electronic structure calculations deliver results appropriate for these states (see Appendix A.4). In the spectroscopic literature, however, the coordinate dependence of the electronic wave functions is difficult to access, and it is more usual to use crude-adiabatic state labels. Yet another approach is to use diabatic state labels, which describe coordinate-dependent single-electron excitations from the ground-state wave function; all such relevant excitations are depicted in Figure 1 and involve transitions from the lone-pair (n) orbital and the two-highest π orbitals to the two-lowest π* orbitals. In general, adiabatic electronic states are comprised of mixtures of these diabatic states, as dictated by the strength of the configuration interaction.

For the (n,π*) transitions, the adiabatic states are dominated by just one diabatic transition, $a_1 \rightarrow b_1$ for $^{1,3}B_1$ and $a_1 \rightarrow a_2$ for $^{1,3}A_2$. However, the (π,π*) states all involve two diabatic states, states whose names we prefix with (α) and (β) as defined in Figure 1; this is a generic feature of (π,π*) spectroscopy, which originates from the pseudo-parity selection rule[53] and is most strongly manifest in the excited states of benzene, which, in D_{6h} symmetry, involve necessarily equal mixtures of the paired excitations. The lower symmetry of pyridine leads to unequal mixing, however, and the contributions of these determinants to the excited state, as calculated using EOM-CCSD, CIS, CASSCF(8,11), and TD-B3LYP, are shown in Table 1. We see that, at the ground-state geometry, the configuration mixing is typically strong. Geometry optimization (within C_{2v} symmetry) has only a minor effect for $^1B_2$ and $^3B_2$ but, for $^3A_1$, produces a double-minimum Born−Oppenheimer potential-energy surface (shown later in Figure 4) with, as shown in Table 1, each minimum corresponding to just one of the two diabatic components; we name these structures $(\alpha)^3A_1$ and $(\beta)^3A_1$ after their dominant component. This effect has been noted previously,[32] but its consequences are yet to be explored. Expressed in terms of crude-adiabatic states, its occurrence is said to indicate strong mixing, or vibronic coupling, between $^3A_1$ and $(2)^3A_1$ as a function of at least one totally symmetric vibrational coordinate. Expressed in terms of diabatic states, this is said to indicate strong electronic coupling between the $(\alpha)^3A_1$ and $(\beta)^3A_1$ diabatic states.

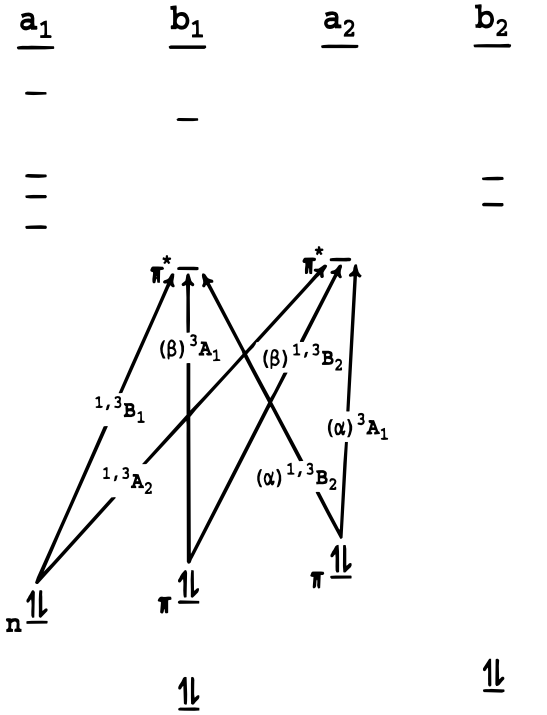

Figure 1. SCF molecular orbitals of pyridine in the range of −0.55 to 0.4 au, and the single-electron excitations which dominate the low-lying excited states.

Standard ab initio and density-functional electronic structure methods evaluate Born−Oppenheimer adiabatic energy surfaces, and indeed, the CASSCF, CASPT2, EOM-CCSD, CIS, and CNDO/S surfaces generated herein are examples of this. However, some intrinsically single-determinate computation methods such as UMP2, CCSD, and direct DFT are also used, and for these, the surfaces generated are actually diabatic. This feature is addressed in more detail in Appendix A.4, but clearly, one must be careful in order to match the computational technique to the required property.

We use the adiabatic labels $^3A_1$ and $(2)^3A_1$ to describe the results of all calculations intended to model these states when strong mixing is involved. The diabatic labels $(\alpha)^3A_1$ and $(\beta)^3A_1$ are used to describe the two minima on the C_{2v} $^3A_1$ Born−Oppenheimer surface, as well as for the crude-adiabatic states used in a simulations of the vibrational−electronic structure of the combined singlet and triplet manifolds, simulations that involve vibronic, electronic, and spin−orbit coupling.

Another important issue of notation concerns the labels used to describe states at geometries of other than C_{2v} symmetry. In most cases, such states can be readily correlated with one particular C_{2v} state, and in these cases we use the C_{2v} description of that state. However, for the lowest-energy triplet Born−Oppenheimer surface, a low-energy structure formed by distortion in out-of-plane b_1 modes is found to correlate with two C_{2v} surfaces, $^3B_1$ and $(\beta)^3A_1$; in this case, we use the more general but less informative $^3A'$ label to describe this structure.

TABLE 1: Amplitudes of the Two Most-Important Single-Electron Excitations (see Figure 1) to the (π,π^*) Excited States of Pyridine[a]

method	config.	$^1B_2$ vert.	$^1B_2$ relax	$^3B_2$ vert.	$^3B_2$ relax	config.	$^3A_1$ vert.	$(\alpha)^3A_1$ relax	$(2)^3A_1$ vert.	$(\beta)^3A_1$ relax
EOM-CCSD	α: $a_2 \rightarrow b_1$	0.55	0.55	0.63	0.65	α: $a_2 \rightarrow a_2$	0.54	0.65	0.41	0.19
	β: $b_1 \rightarrow a_2$	−0.38	−0.35	0.24	0.20	β: $b_1 \rightarrow b_1$	−0.40	−0.16	0.53	0.64
TD-B3LYP	α: $a_2 \rightarrow b_1$	0.87	0.90	0.93	0.93	α: $a_2 \rightarrow a_2$	0.66	0.79	0.58	0.17
	β: $b_1 \rightarrow a_2$	−0.48	−0.44	0.16	0.13	β: $b_1 \rightarrow b_1$	−0.15	−0.44	0.77	0.53
CIS	α: $a_2 \rightarrow b_1$	0.60	−0.36	0.68	0.69	α: $a_2 \rightarrow a_2$	0.52	0.64	0.46	
	β: $b_1 \rightarrow a_2$	0.62	−0.34	0.15	0.12	β: $b_1 \rightarrow b_1$	−0.44	−0.24	0.53	
CASSCF	α: $a_2 \rightarrow b_1$	0.71	−0.53	0.85	0.85	α: $a_2 \rightarrow a_2$	0.56	0.59	0.56	0.26
	β: $b_1 \rightarrow a_2$	0.71	−0.52	0.37	0.36	β: $b_1 \rightarrow b_1$	−0.37	−0.31	0.72	0.89

[a] Evaluated either at the ground-state equilibrium geometry (vert.) or at the C_{2v}-optimized geometry of the excited state (relax); $(\alpha)^3A_1$ and $(\beta)^3A_1$ are the two local minima on the lower $^3A_1$ adiabatic surface.

TABLE 2: RMS Deviations from Experiment for Calculated Properties of the Ground State $^1A_1$ (S_0) of Pyridine[a]

				vibrations	
method	basis set	R/Å	θ/degrees	scale[d]	ν/cm^{-1}
MP2	cc-pVDZ	0.012	0.31	0.9434	30
CCSD	cc-pVDZ	0.012	0.27	0.9500	23
CCSD(T)	cc-pVDZ	0.015	0.38	0.9500	32
CASSCF(8/11)	cc-pVDZ	0.002	0.23	0.9100	37
CASSCF(8/7)[b]	6-31G**	0.008	0.29	0.9100	34
B3LYP	cc-pVDZ	0.007	0.07	0.9614	23
BLYP	cc-pVDZ	0.016	0.21	0.9945	21
SCF	cc-pVDZ	0.007	0.27	0.8935	36
B3LYP[c]	cc-pVTZ	0.003	0.19	0.9614	17

[a] Averaged over the six unique bond lengths R, the seven unique bond angles θ, and all 27 vibrational frequencies ν; full details are given in the Supporting Information. [b] From ref 9. [c] From ref 10. [d] All (ground-state) vibration frequencies are scaled by this factor.[54]

3. Results of the Electronic Structure Calculations

In this section, we consider the molecular properties that are straightforward to evaluate using electronic structure calculations, such as vertical excitation energies, equilibrium geometries, relaxation energies, and harmonic vibration frequencies, possibly including corrections for diagonal anharmonicity. These data will be used in section 4 to simulate the observed electronic spectra. Here, we determine the reliability of the various computational methods in order to gauge the extent through which the calculated parameters can be varied in order to fit the experimental spectra. Also, some molecular properties are well-known experimentally, whereas others are poorly established, and it is our aim to classify the experimental data. Indeed, revised assignments obtained in section 4 through explicit simulation of the experimental spectra are also included.

3.1. The Ground-State X $^1A_1$. The geometry and vibrational frequencies of the ground state of pyridine have previously been calculated using CASSCF,[8,9] B3LYP,[10] MP2,[11] and other methods, and excellent results obtained. In our context, a consideration of properties calculated for this state is important in that any computational method that is to be applied to excited state potential-energy surfaces must first be shown to provide a good description of the ground state. In Table 2, a summary is provided of the performance of the methods that we later employ for excited states, plus that of closely related methods and results obtained from the literature, for the average deviation of the calculated bond lengths, bond angles, and scaled[54] vibrational frequencies from the experimental[1] values. Full details of the optimized geometries and normal modes are given in Supporting Information. *All* of the calculated results are seen to be in excellent agreement with experiment: the root-mean-square (RMS) errors ranging from 0.002 to 0.016 Å for bond lengths, from 0.07 to 0.38° for bond angles, and from 17 to 37 cm^{-1} for vibration frequencies. The methods used are SCF, MP2, CASSCF, CCSD, CCSD(T), BLYP, and B3LYP.

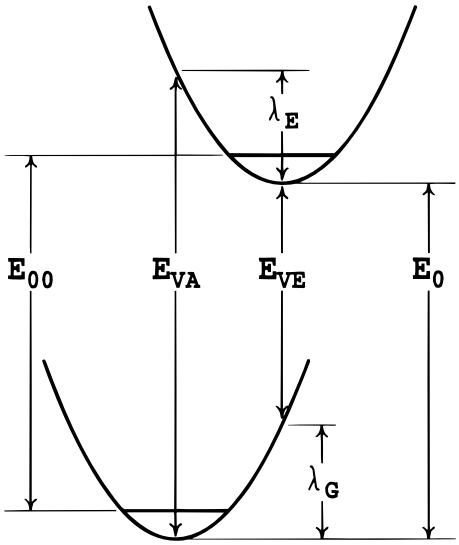

Figure 2. Definition of the vertical excitation energy E_{VA}, the vertical emission energy E_{VE}, the ground and excited-state reorganization energies λ_G and λ_E, the adiabatic energy difference E_0, and the lowest transition energy E_{00}.

3.2. Vertical Excitation Energies. Table 3 shows the calculated vertical excitation energies from the ground state for the eight excited states of interest, together with assignments to observed values and the results of previous calculations. In total, assignments for the $^1B_1$, $^1A_2$, $^1B_2$, $^3A_1$, $(2)^3A_1$, $^3A_2$, and $^3B_2$ states are provided, but of these, unequivocal experimental assignments[1,20] are available only for the lowest two singlet states, and the other assignments are heavily based on computational results. It is thus most important that the best-possible values are obtained for the experimental vertical excitation energies through interpretation of the available low-resolution spectra. Proper treatment of zero-point vibration is also essential.

3.2.1. Experimental Values. Figure 2 shows two generic potential-energy surfaces and indicates the vertical excitation energy E_{VA}, defined as the energy of the excited state at the geometry of the ground state; the analogous vertical emission energy E_{VE}; the adiabatic energy difference E_0; the ground and excited-state reorganization energies λ_G and λ_E, respectively; the ground and excited-state zero-point energy (ZPT) levels; and the 0−0 transition energy E_{00}. The vertical excitation energy corresponds roughly to the absorption band maximum, and it is most common to compare calculated vertical energies E_V (= E_{VA} or E_{VE}) to experimental band maxima. More precisely, these correspond to zero-point-energy-corrected average transition energies

TABLE 3: Calculated and Observed Vertical Excitation Energies, E_{VA}, in eV, for Pyridine

method	basis set	$^1B_1$ (S_1) (n,π^*)	$^1A_2$ (S_3) (n,π^*)	$^1B_2$ (S_2) (π,π^*)	$^3A_1$ (π,π^*)	(2)$^3A_1$ (π,π^*)	$^3B_1$ (n,π^*)	$^3A_2$ (n,π^*)	$^3B_2$ (π,π^*)	RMS error
CCSD(T)	cc-pVDZ				4.47		4.59		5.01	0.15
CCSD(T)	cc-pVTZ				4.45				4.87	0.11
CCSD(T)	aug-cc-pVDZ				4.44		4.54		4.85	0.10
CCSD	cc-pVDZ				4.32	4.65	4.49	5.55	4.98	0.15
CCSD	cc-pVTZ				4.28		4.46		4.80	0.07
CCSD	aug-cc-pVDZ				4.29		4.45		4.80	0.06
EOM-CCSD	cc-pVDZ	5.29	5.69	5.29	4.06	5.12	4.63	5.62	4.90	0.21
EOM-CCSD	aug-cc-pVDZ	5.19		5.19	4.04		4.58		4.76	0.21
CASSCF(8,11)	cc-pVDZ	5.68	6.37	5.20	4.08	5.25	5.09	6.36	5.06	0.56
CASSCF(8,11)	aug-cc-pVDZ	5.69		5.22	4.08		5.12		5.05	0.42
CASPT2	cc-pVDZ	5.00	5.25	4.89	4.10	4.77	4.37	5.22	4.61	0.23
CASPT2	aug-cc-pVDZ	4.93		4.88	4.06		4.31		4.52	0.25
CIS	cc-pVDZ	6.19	7.39	6.31	3.54	5.13	5.12	7.14	4.82	1.18
TD-B3LYP	cc-pVDZ	4.83	5.09	5.58	3.90	4.89	4.06	4.94	4.57	0.38
TD-BLYP	cc-pVDZ	4.39	4.44	5.29	4.07	4.74	3.72	4.32	4.41	0.68
B3LYP	cc-pVDZ				4.42	4.75	4.29	5.13	4.70	0.24
BLYP	cc-pVDZ				4.37	4.66	4.16	4.86	4.57	0.39
SAC-CI[a]	DZ+d+p[b]	5.24	5.69	5.44	4.34	5.32	4.49	5.69	5.09	0.26
MRCI[c]	DZ+d[d]	4.50	5.36	4.76	3.95	4.93	3.87	5.43	4.98	0.26
CASSCF[e]	ANO[f]	5.26	5.96	5.04	4.13	4.93	4.82	6.80	4.80	0.54
CASPT2[e]	ANO[f]	4.91	5.17	4.84	4.05	4.73	4.41	5.10	4.56	0.29
EOM-CCSD[h]	Sadlej[j]	5.17	5.61	5.22						0.17
EOM-CCSD(T)[h]	Sadlej[j]	4.80	5.24	4.81						0.25
STEOM-CCSD[k]	Sadlej[j]	4.91	5.31	4.82	3.73	4.90	4.32	5.31	4.68	0.28
CIS[l]	6-31G*	6.25	7.24	6.30	3.65	5.20	5.21	7.18	4.87	1.16
observed-raw		4.74[g]	5.43[c]?	4.99[m]	4.1[c]?	4.84[c]?		5.43[c]?	4.84[c]?	–
observed-ZPE-corrected		4.90	5.52	5.13	4.3	4.93		5.52	4.89	–

[a] From ref 31. [b] Huzinaga and Dunning's double-ζ plus diffuse and polarization functions (total 98 functions), see ref 31. [c] From ref 20, with ? indicating that the assignment (to peaks observed in electron energy loss spectra) is based purely on computational data. [d] Huzinaga and Dunning's double-ζ plus diffuse functions (total 91 functions), see ref 20. [e] From refs 8 and 36. [f] Large atomic natural orbital basis, see ref 36. [g] Our analysis (see text) of the observed[15] fluorescence excitation spectrum. [h] From ref 37. [j] 189 basis functions, from ref 75. [k] From ref 38. [l] From ref 34. [m] From ref 14.

$$E_V = \frac{\int_0^\infty S(\nu)\, h\nu \, d\nu}{\int_0^\infty S(\nu)\, d\nu} - \Delta E_{ZPT} \qquad (1)$$

where $S(\nu)$ is the Franck−Condon-allowed component of the bandshape function, which is ϵ/ν for absorption or fluorescence excitation and ϵ/ν^3 for fluorescence or phosphorescence, with ϵ the molar extinction/emission at frequency ν and ΔE_{ZPT} is the change in zero-point (ZPT) energy between the initial and final states. As ΔE_{ZPT} is not usually available experimentally, it would appear most appropriate to compare average observed transition energies to theoretically evaluated $E_V + \Delta E_{ZPT}$. However, ΔE_{ZPT} is expensive to compute, and we have evaluated it only for a small fraction of the computational methods that we consider. Hence, we average ΔE_{ZPT} over all of the methods used, and use this to correct the experimentally observed average frequencies. The results are shown in Table 3, while the calculated zero-point correction energies are shown in Table 4.

Figure 3 shows the observed[15] low-resolution gas-phase absorption spectrum of pyridine. Absorption to the lowest singlet excited state, $^1B_1$ (S_1), is weak and appears only as a shoulder on the much stronger $^1B_2$ (S_2) absorption. However, as the fluorescence quantum yield from $^1B_1$ following excitation into $^1B_2$ is 2 orders of magnitude lower than that following direct excitation,[15,17] the fluorescence excitation spectrum provides a realistic model of the $^1B_1$ absorption spectrum, and this spectrum[15] is also shown in Figure 3. This is the spectrum that we analyze in order to estimate the vertical excitation energy of $^1B_1$. Extrapolating the observed[15] fluorescence excitation spectrum to zero signal, we estimate that the vertical excitation energy for $^1B_1$ is 4.74 eV, and this value is shown in Table 3. It is clearly consistent with the theoretical predictions. However, the observed band receives significant intensification from non-Condon effects, particularly on the low-frequency side, while emission from S_2 is likely to contribute to the high-frequency side. Hence, this estimate is still quite approximate.

Although the observed singlet-state absorption spectrum[15] shown in Figure 3 is dominated by absorption to S_2, extraction of the average absorption frequency for S_2 using eq 1 is hampered by the presence of overlapping bands to both low and high frequency. Shown in Table 3 is simply the value[14] of the band maximum, 4.99 eV, and this value would appear to approximate the location of the average absorption frequency to within 0.1 eV.

3.2.2. Assignments. From experimental evidence,[1] the assignment of the above-mentioned $^1B_1$ (S_1) and $^1B_2$ (S_2) bands is quite clear; for all other states, the assignment is not so straightforward. Three bands are seen in the near-threshold electron energy loss spectra of pyridine[20] at 4.1, 4.84, and 5.43 eV (see later in Figure 8). These bands have been assigned[8,20,36,37] to one or more of six likely electronic states purely on the basis of computed vertical excitation energies, and our results concur with these assignments. The high-quality computational methods all predict that the $^1A_2$ and $^3B_2$ states are located in the region of 5.4 eV and are split by less than 0.1 eV in energy, and it is clear[20] that the observed 5.43 eV band originates from one or quite likely both of these states. Also, most computational methods predict that the (2)$^3A_1$ and $^3A_2$ bands lie close to the observed peak at 4.84 eV, and it is unclear as to whether it originates from one or both of these states. Finally, the observed peak at 4.1 eV could conceivably arise from one or both of the $^3A_1$ and $^3B_1$ states. CCSD(T) predicts that $^3A_1$ (π,π^*) lies 0.1 eV vertically below $^3B_1$ (n,π^*), but because of the multiconfigurational nature of $^3A_1$ at this geometry (see Table 1), the energy for this state is likely to be inaccurate. STEOM-CCSD and EOM-CCSD calculations predict $^3A_1$ to be ca. 0.6 eV lower than $^3B_1$, whereas this magnitude is

TABLE 4: Calculated Changes $E_{00} - E_0$ to the 0−0 Excitation Energies of Pyridine Arising from Zero-Point Vibrational Motion, in eV[a]

	$^1B_1$ (n,π^*)		$^1A_2$ (n,π^*)	$^1B_2$ (π,π^*)	$(\alpha)^3A_1$ (π,π^*)	$(\beta)^3A_1$ (π,π^*)	$^3B_1$ (n,π^*)	$^3A'$ (mixed)	$^3A_2$ (n,π^*)	$^3B_2$ (π,π^*)
method	C_{2v}	C_s	C_{2v}	C_{2v}	C_{2v}	C_{2v}	C_{2v}	C_s	C_{2v}	C_{2v}
CASSCF(8/11)	−0.11	−0.14	−0.14	−0.11	−0.20	−0.20	−0.12	−0.17	−0.07	−0.07
CCSD								−0.19		
EOM-CCSD	−0.20	−0.18	−0.04	−0.16						
B3LYP					−0.25	−0.21	−0.17	−0.16	−0.11	−0.01
BLYP					−0.22	−0.11	−0.18	−0.17	0.12[b]	−0.06
average	−0.16	−0.16	−0.09	−0.14	−0.22	−0.17	−0.16	−0.18	−0.09	−0.05

[a] For states whose minimum is of low symmetry, values at the C_{2v}-optimized geometry are also listed and were obtained using numerical calculations to estimate the zero-point energy associated with the modes of imaginary frequency. All calculations are performed using the cc-pVDZ basis set. The CASSCF(8,11) result for $(2)^3A_1$ is −0.09 eV. [b] Not used in average.

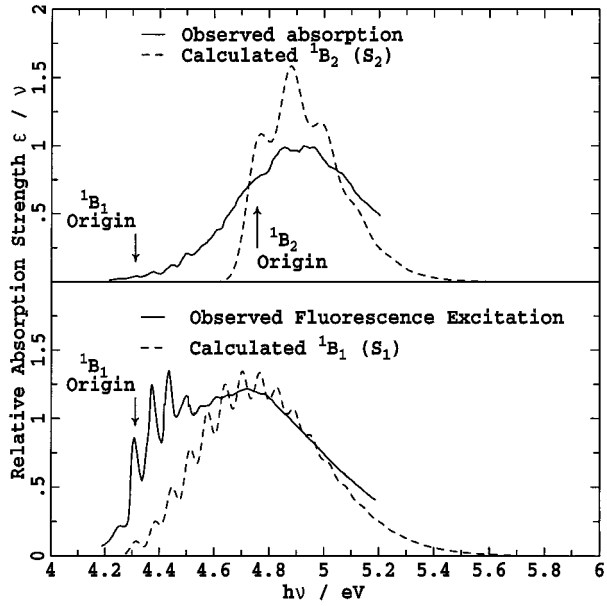

Figure 3. The upper frame shows the observed low-resolution gas-phase absorption spectrum of pyridine[15] and the calculated spectrum for $^1B_2$ (S_2), while the lower frame shown the observed fluorescence excitation spectrum[15] and the calculated electronically allowed absorption spectrum for $^1B_1$ (S_1). The spectra are normalized to constant area.

ca. 0.3 eV for CASPT2; alternatively, the density-functional methods predict energy differences ranging from −0.16 to +0.35 eV, whereas (older) MRCI calculations[20] predict +0.08 eV. However, the observed lack of solvent dependence for the singlet-to-triplet absorption band[22] is clear evidence that this band is (π,π^*). In section 4.3, we model the vibrational structure of the gas-phase high-resolution singlet-to-triplet absorption spectrum and show conclusively that the 4.1 eV band is, in, fact due to $^3A_1$.

3.3. Relaxation of Excited-State Geometries within C_{2v} Symmetry. *3.3.1. Experimental Reorganization Energies.* The geometries of the eight excited states considered were optimized using a variety of computational methods; resulting key geometrical properties are given in Tables 5 and 6, all reorganization energies λ_E (see Figure 2) are given in Table 7, while the corresponding adiabatic energy differences E_0 are given in Table 8. All results are provided in full in Supporting Information. The experimental reorganization energies are evaluated from the observed absorption bands using the equation

$$\lambda_E = \frac{\int_0^\infty S(\nu)\, h\nu \, d\nu}{\int_0^\infty S(\nu)\, d\nu} - E_{00} \qquad (2)$$

where E_{00} is the observed origin energy.

The most reliable experimental data is available for the $^1B_1$ (n,π^*) (S_1) and $^1B_2$ (π,π^*) (S_2) states, for which the reorganization energies are 0.43 and 0.23 eV, respectively. Although the origin frequencies are very well-known, considerable uncertainty in these quantities does arise through the aforementioned

TABLE 5: Key Calculated Geometrical Parameters for the Electronic States of Pyridine[a]

state	method	symm.	R_{N-C2}	R_{C2-C3}	R_{C3-C4}	$\theta_{C2-N-C2}$	$\theta_{N-C2-C3}$	$\theta_{C2-C3-C4}$	$\theta_{C3-C4-C3}$
$^1A_1(S_0)$	CCSD	C_{2v}	1.346	1.405	1.403	116	124	118	118
$^1B_1(S_1)$	EOM-CCSD	C_{2v}	1.369	1.387	1.434	129	115	121	119
$^1B_1(S_1)$	EOM-CCSD	C_s	1.371	1.389	1.433	127	114	120	119
$^1B_1(S_1)$	CASSCF	C_s	1.385	1.370	1.441	125	114	119	119
$^1B_1$-$^1A_2$ CI	CASSCF	C_{2v}	1.332	1.433	1.386	133	113	118	123
$^1A_2(S_3)$	CASSCF	C_{2v}	1.319	1.458	1.396	135	113	118	124
$^1A_2(S_3)$	EOM-CCSD	C_{2v}	1.313	1.478	1.400	136	113	117	124
$^1B_2(S_2)$	EOM-CCSD	C_{2v}	1.380	1.438	1.437	113	126	120	115
$(\alpha)^3A_1$	CCSD	C_{2v}	1.338	1.532	1.398	118	123	118	119
$(\alpha)^3A_1$	CASSCF	C_{2v}	1.336	1.508	1.395	118	123	118	119
$(\alpha)^3A_1$−$(\beta)^3A_1$ TS	CASSCF	C_{2v}	1.385	1.405	1.447	117	124	119	117
$(2)^3A_1$	CASSCF	C_{2v}	1.372	1.423	1.440	117	124	119	117
$(\beta)^3A_1$	CASSCF	C_{2v}	1.409	1.365	1.470	116	124	120	116
$(\beta)^3A_1$	CCSD	C_{2v}	1.436	1.357	1.483	114	125	120	116
$^3B_1$	CCSD	C_{2v}	1.381	1.383	1.432	128	116	121	118
$(\alpha)^3A_1$−$^3B_1$ CI	CASPT2[b]	C_{2v}	1.367	1.428	1.422	125	118	120	119
$(\beta)^3A_1$−$^3B_1$ CI	CASPT2[b]	C_{2v}	1.400	1.373	1.452	123	119	121	117
$^3A'$	CCSD	C_s	1.420	1.372	1.446	115	116	119	118
$^3A_2$	CCSD	C_{2v}	1.315	1.481	1.402	136	113	117	124
$^3B_2$	CCSD	C_{2v}	1.377	1.435	1.428	110	127	122	112

[a] Bond lengths, R, in Å and angles, θ, in degrees; full coordinates are given in Supporting Information. CI indicates a conical intersection, TS indicates a transition state. [b] Estimated by evaluating the CASPT2 energies of the intersecting states along a section linearly interpolated between the appropriate C_{2v} CCSD-optimized geometries.

TABLE 6: Distortion Angles for Boatlike Structures of the (2)^{1}A′ ≡ ^{1}B$_1$ (n-π*) and ^{3}A′ (mixed n-π* and π-π*) States of Pyridine, in Degrees[a]

state	method	basis set	θ	ϕ
^{1}B$_1$	EOM-CCSD	cc-pVDZ	27.1	9.0
	CASSCF(8/11)	cc-pVDZ	33.0	12.1
	CIS	cc-pVDZ	31.4	6.7
^{3}A′	CCSD	cc-pVDZ	40.6	11.5
	CASSCF(8/11)	cc-pVDZ	2.3	12.2
	TD-BLYP	cc-pVDZ	35.5	10.1
	B3LYP	cc-pVDZ	38.2	9.6
	BLYP	cc-pVDZ	37.1	8.6
	BLYP	aug-cc-pVDZ	37.3	8.8
	MRDCI[b]	6-31G	∼35	∼10
	UHF[c]	3-21G	38.2	9.9
	UMP2[c]	STO-3G	39.8	14.4
	UMP2	cc-pVDZ	37.6	13.8
	UMP2	aug-cc-pVDZ	37.5	14.3
	obs.[d]		40	10

[a] θ indicates out-of-plane bending of the nitrogen, while ϕ indicates that for the para carbon, see Figure 5. [b] From ref 33. [c] From ref 32. [d] From ref 27.

difficulties in determining the average absorption frequency. The EOM-CCSD, CASSCF(8,11), CASPT2, TD-B3LYP, and TD-BLYP computational methods reproduce λ_E to within 0.08 eV, whereas the CASSCF and CIS methods produce errors of up to twice this magnitude. As these errors are on the order of 10% of the largest relaxation energies calculated, we see that the calculated reorganization energies are sufficiently reliable to permit semiquantitative analysis of the excited states.

3.3.2. The $^1B_1$−$^1A_2$ Conical Intersection. An interesting result is that relaxation has a large effect on the energies of the ^{1}A$_2$ and ^{3}A$_2$ (n,π*) states, with all methods predicting $0.7 < \lambda_E < 1.0$ eV. This effect was first noticed by Lorentzon, Fülscher, and Roos[8] for ^{1}A$_2$ and is significant in that the relaxations of these states are much larger than those for slightly lower-energy states ^{1}B$_1$ (ca. 0.4−0.5 eV) and ^{1}B$_2$ (ca. 0.2 eV). In fact, the quality calculations predict that the minimum of ^{1}A$_2$ (S$_3$) lies from between 0.22 eV lower to 0.04 eV higher in energy than that for ^{1}B$_1$ (S$_1$). Experimentally, it is unlikely that ^{1}A$_2$ is actually the lowest-energy singlet excited state as no evidence suggesting this has been found in high-resolution fluorescence studies, and some emission would be expected from ^{1}A$_2$ because of vibronic coupling with other excited states. Similarly, no role has been postulated for this state in the interpretation of the excited-state femtosecond dynamics of pyridine.[2]

To explore this issue further, we optimized the geometry of the ^{1}B$_1$−^{1}A$_2$ conical intersection (CI) using state-averaged CASSCF(8,6) calculations (all b$_2$ orbitals are excluded from this active space, see Appendix A.2), and the results are included in Table 5 and the Supporting Information. Fortunately, the error introduced by using this reduced active space tends to cancel the CASPT2 correction, and at this geometry, the CASPT2(8,-11) energies above the ground-state minimum are 4.81 and 4.54 eV for ^{1}B$_1$ and ^{1}A$_2$, respectively. Although this geometry is possibly somewhat distorted from the true CASPT2(8,11) geometry, the important feature is that both energies are less than the corresponding vertical excitation energies, and in fact, the energy for ^{1}A$_2$ is only 0.10 eV above the calculated minimum for that state. Further, the geometries shown in Table 5 are similar, as both transitions are (n,π*), with the bond lengths for the CI being intermediary and, as such, more similar to those for the ground state. We also estimated the location of the CI by evaluating the CASPT2(8,11) energy along a section linearly interpolated between the CASSCF-optimized geometries of ^{1}B$_1$ and ^{1}A$_2$. The two surfaces crossed at a geometry that was 60% that of ^{1}B$_1$ at an energy of 4.57 eV, a result that is very similar to the previous one. Hence, we conclude that the CI lies at low energy in the Franck−Condon region, and it is thus expected to actually have a significant influence on excited-state dynamics.

3.3.3. Pseudo-Parity Breaking in the Lowest Triplet (π,π) State.* Relaxation of the ^{3}A$_1$ (π,π*) state leads to a double-well potential, with normal-mode analysis (see results in Supporting Information) indicating that the most important difference between the two minima is a displacement in ν_{8a}, the totally symmetric vibration observed[1] in the ground state at 1599 cm^{-1}. This scenario results from decoupling of the two single configurations named α and β in Table 1 and Figure 1, as described in section 2, and the corresponding minima are named (α)^{3}A$_1$ and (β)^{3}A$_1$, respectively. Relevant potential-energy curves, shown as a function of the linear displacement between the two minima (projected onto the ground-state dimensionless normal coordinate Q_{8a}), are given in Figure 4. Electronic structure methods such as CCSD, B3LYP, and BLYP do not fully include the configuration interaction between these states

TABLE 7: Calculated and Observed Excited-State Reorganization Energies λ_E, in eV, for Electronic Transitions between Various Excited States and the Ground State of Pyridine[a]

	^{1}B$_1$ (n,π*)		^{1}A$_2$ (n,π*)		^{1}B$_2$ (π,π*)		(α)^{3}A$_1$ (π,π*)		(β)^{3}A$_1$ (π,π*)		^{3}B$_1$ (n,π*)		^{3}A$_2$ (n,π*)		^{3}B$_2$ (π,π*)	
method	sym.	asym.	sym.	asym.	sym.	asym.	sym.	asym.	sym.	asym.[h]	sym.	asym.[h]	sym.	asym.	sym.	asym.
CCSD							0.57	0	0.41	0.21$^{\perp}$	0.46	0.34$^{\perp}$	0.85		0.22	
EOM-CCSD	0.47	0.017$^{\perp}$	0.85	[0.010]$^{\parallel}$	0.18	[0.007]^2	0.32[e]	[0.0004]$^{\parallel}$	0.11[e]	0.18$^{\perp}$	0.45[e]	0.42$^{\perp}$	0.83	[0.112]$^{\parallel}$	0.18[e]	
CASSCF(8,11)	0.56	0.011$^{d\perp}$	0.78	[0.071]$^{d\parallel}$	0.25	0	0.41	∼0[d]	0.21	[0.017]$^{d\parallel}$	0.47	0.04$^{d\perp}$	0.80	0	0.19	0
CASPT2[b]	0.51[c]	0.040$^{d\perp}$	0.81	[0.004]$^{d\parallel}$	0.34	0	0.39	∼0[d]	0.20		0.46	0.04$^{d\perp}$	0.82	0	0.30	0
CASPT2[e]										0.19$^{d\perp}$	0.45	0.21$^{d\perp}$				
CIS	0.59	0.042$^{\perp}$	1.05		0.09	[0.038]^2	0.22	[0.007]$^{\parallel}$			0.52	0	1.01	0	0.12	0
TD-B3LYP	0.43	0	0.77	[0.002]$^{\parallel}$	0.17	0	0.40		0.22	0.33$^{\perp}$	0.40	[0.31]$^{\perp}$	0.76	[0.066]$^{\parallel}$	0.21	
TD-BLYP	0.43	0	0.70	0	0.19	0	0.41		0.21	[0.016]$^{\parallel}$	0.38	0.084$^{\perp}$	0.69	[0.007]$^{\parallel}$	0.21	
B3LYP							0.58	[0.004]^2	0.32	0.44$^{\perp}$	0.42	0.20$^{\perp}$	0.80	[0.066]$^{\parallel}$	0.22	[0.0002]$^{\perp}$
BLYP							0.54	[0.035]^2	0.29	[0.016]$^{\parallel}$	0.37	0.20$^{\perp}$	0.76	[0.007]$^{\parallel}$	0.21	[0.0002]$^{\perp}$
MRDCI												[0.19]$^{\perp}$				
Total Obs.[f]	0.43	0.001			0.23		0.4[g]		0.2[g]	0.3−0.4[g]						

[a] Evaluated using the cc-pVDZ basis set and separated into contributions from totally symmetric and antisymmetric modes; antisymmetric distortion lowers the point-group symmetry from C_{2v} to either C_2 from a$_2$ distortion, $C_{s\parallel}$ (retaining molecular plane) from b$_2$ distortion, $C_{s\perp}$ (boatlike with the molecule nonplanar) from b$_1$ distortion, and C_1 from multiple distortion, and these cases indicated by superscripts 2, ∥, ⊥, and n, respectively. Values in brackets are lower bounds estimated considering only the contributions from the modes of imaginary frequency detailed later in Table 16. [b] At the CASSCF-optimized geometry. [c] Value is[8,36] 0.54 eV using a Sadlej[75] basis set. [d] CASSCF energy discontinuous, see text and Table 11. [e] At CCSD/cc-pVDZ geometry. [f] Raw data from refs 1, 3, 14, 20, 21, and 29. [g] Our assignment, see text. [h] ⊥ (b$_1$) distortion leads to the boatlike ^{3}A′ structure.

TABLE 8: Calculated Adiabatic Energy Differences E_0 to the Ground State of Pyridine, in eV

method	basis set	$^1B_1$ (n,π^*) C_s	$^1A_2$ (n,π^*) C_{2v}	$^1B_2$ (π,π^*) C_{2v}	(α)$^3A_1$ (π,π^*) C_{2v}	(β) $^3A_1$ (π,π^*) C_{2v}	$^3B_1$ (n,π^*) C_{2v}	$^3A'$ (mixed) C_s	$^3A_2$ (n,π^*) C_{2v}	$^3B_2$ (π,π^*) C_{2v}
CCSD	cc-pVDZ				3.75	3.91	4.04	3.70	4.70	4.76
CCSD[b]	aug-cc-pVDZ				3.72		3.96	3.64		4.59
CCSD(T)[b]	cc-pVDZ				3.90	4.09	4.12	3.82		4.76
CCSD(T)[b]	aug-cc-pVDZ				3.87		4.06	3.75		4.60
EOM-CCSD	cc-pVDZ	4.80	4.84	5.11	3.74	3.95	4.19	3.77	4.79	4.72
EOM-CCSD[b]	aug-cc-pVDZ	4.68		5.00	3.72		4.12			4.58
CASSCF(8/11)	cc-pVDZ	5.11	5.59	4.95	3.67	3.87	4.62	3.58	5.56	4.86
CASPT2[a]	cc-pVDZ	4.45	4.44	4.55	3.71	3.90	3.91	3.95	4.40	4.31
CASPT2[a]	aug-cc-pVDZ	4.41	4.32	4.67	3.56		3.83	3.88	4.29	4.21
CASPT2[b]	cc-pVDZ	4.45		4.56	3.73	3.90	3.92	3.71		4.33
CASPT2[b]	aug-cc-pVDZ	4.43		4.57	3.66		3.84	3.64		4.13
CIS	cc-pVDZ	5.57	6.34	6.22	3.32		4.60	–	6.13	4.70
TD-B3LYP	cc-pVDZ	4.40	4.31	5.41	3.50	3.68	3.66	3.35[c]	4.18	4.36
TD-BLYP	cc-pVDZ	3.96	3.74	5.10	3.66	3.86	3.34	3.26	3.63	4.20
B3LYP	cc-pVDZ				3.84	4.10	3.86	3.66	4.33	4.48
BLYP	cc-pVDZ				3.83	4.08	3.79	3.59	4.10	4.36
Obs.[d] E_{00}		4.31		4.76	3.68[f]	3.93[f]		3.56−3.62[f]		
Obs.[e] E_0		4.47		4.90	3.90[f]	4.10[f]		3.74−3.80[f]		

[a] At CASSCF-optimized geometry. [b] At CCSD-optimized geometry. [c] At TD-BLYP-optimized geometry. [d] Observed 0−0 energies.[1] [e] Adjusted for the average calculated zero-point energy correction from Table 4. [f] Our assignment, see text.

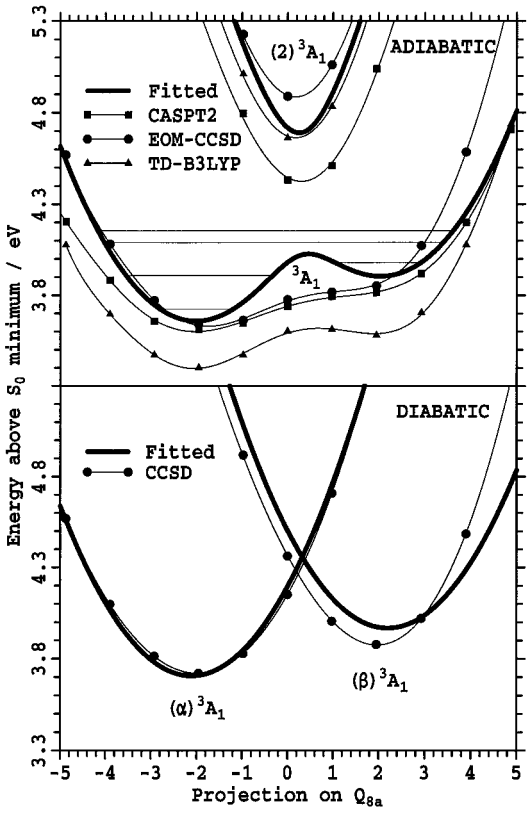

Figure 4. Potential energy of the low-lying $^3A_1$ states of pyridine a function of linear motion through the CCSD-calculated (α)$^3A_1$ and (β)$^3A_1$ minima projected onto the ground-state dimensionless normal coordinate Q_{8a}. The upper frame shows adiabatic TD-B3LYP, CASPT2, EOM-CCSD, and fitted surfaces for $^3A_1$ and (2)$^3A_1$, indicating also the lowest five vibrational levels of the fitted surface that involve Q_{8a}. The lower frame shows the corresponding diabatic fitted and CCSD surfaces for (α)$^3A_1$ and (β)$^3A_1$.

and, in fact, produce diabatic rather than adiabatic surfaces (see Appendix A.4). Those obtained using CCSD are shown in this figure and clearly depict two independent local minima. Adiabatic surfaces produced using the CASSCF(8,11), TD-B3LYP, and TD-BLYP also indicate that $^3A_1$ has two minima, and the structure of the linking transition state, optimized using state-averaged CASSCF(8,11), is given in Table 5 and the Supporting Information. However, the computed surface sections shown in Figure 4 reflect much stronger coupling between the diabatic states, and for CASPT2 and EOM-CCSD, the transition state is suppressed with only one minimum apparent, while the second minimum is present but very shallow for TD-B3LYP. Finally, also shown in Figure 4 are the adiabatic surfaces for (2)$^3A_1$ obtained using CASPT2 and EOM-CCSD. These differ from each other by a surprisingly large amount, 0.5 eV. The $^3A_1$ and (2)$^3A_1$ Born−Oppenheimer surfaces may be said to arise either through electronic coupling of the (α)$^3A_1$ and (β)$^3A_1$ diabatic states or, alternatively, through strong vibronic coupling in mode ν_{8a} between the $^3A_1$ and (2)$^3A_1$ crude-adiabatic states.

Shown in Table 7 are actually the reorganization energies λ_E obtained as the difference of the vertical excitation energy of $^3A_1$ and the energies of the two local minima, (α)$^3A_1$ and (β)$^3A_1$. Experimentally, singlet-to-triplet absorption spectra have been observed in both solution[22] and high-resolution gas-phase[21] spectroscopy. We assign these spectra in section 4.3, determining the energy of the origin transitions, and the results are shown in Tables 7 and 8. From Table 7, it is clear that the calculated reorganization energies support these assignments.

3.4. Relaxations that Lower the Point-Group Symmetry. The antisymmetric-mode relaxation energies shown in Table 6, when greater than zero, indicate the energy difference between the lowest-energy structure of C_{2v} symmetry and local minimum structures of lower symmetry. For the important distortions, these values were obtained through geometry optimization; otherwise, the relaxation energies were estimated by sectioning the potential surface linearly in the direction of the normal modes of imaginary frequency. The sectioning technique provides a lower bound to the actual reorganization energy. It is reliable when only small angle changes are involved; otherwise, anharmonic and possibly also Duschinsky rotation effects become pronounced. Overall, quite a large variation in the calculated results are found, as these relaxations, which can be attributed to vibronic coupling effects, are very sensitive to the calculated energy spacings between the electronic states.[55]

3.4.1. The Boat Structure of $^3B_1$. Historically, there has been much interest concerning distortions of the $^1B_1$ and $^3B_1$ (n,π^*) states. For this triplet state, Buma et al.[33] using MRDCI, as well as Nagaoka and Nagashima[32] using UHF and UMP2 have demonstrated it to be distorted along the b_1 normal coordinate

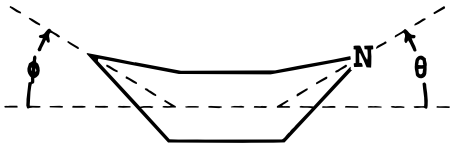

Figure 5. Structure of pyridine in its C_s boat conformation.

TABLE 9: Calculated (B3LYP/cc-pVDZ) and Observed (in Benzene Crystal at 1.2 K) Excess Alpha Spin Densities for Triplet States of Pyridine

state	symm.	N	C_{ortho}	C_{meta}	C_{para}
$(\alpha)^3A_1$ (π,π^*)	C_{2v}	−0.19	0.62	0.64	−0.23
$(\beta)^3A_1$ (π,π^*)	C_{2v}	0.78	0.06	0.14	0.89
$^3B_1$ (n,π^*)	C_{2v}	1.13	0.22	−0.03	0.47
$^3A'$ (mixed)	C_s	1.05	0.25	−0.06	0.55
$^3A_2$ (n,π^*)	C_{2v}	0.69	0.21	0.48	−0.15
$^3B_2$ (π,π^*)	C_{2v}	0.33	0.35	0.32	0.41
obs.[a]	C_s	1.0	0.2	0.0	0.6

[a] From refs 26 and 27.

of ν_{16b}, attaining the boatlike configuration shown in Figure 5. This distortion can be characterized in terms of the two torsional angles θ (for N bending) and ϕ (for para C bending) depicted in the figure, and results obtained using various computational methods are given in Table 6. Almost all methods predict that $35° < \theta < 41°$ and $9° < \phi < 14°$, in excellent agreement with the observed electron-spin-resonance geometry for the equilibrated triplet-state manifold of pyridine in benzene crystal[27] of 40° and 10°, respectively. The only method not to predict this geometry was CASSCF(8,11), for which $\theta = 2°$. A large range of antisymmetric-mode reorganization energies is predicted, from 0.04 eV (CASSCF) to 0.08−0.31 eV (DFT) to 0.34 eV (CCSD) to 0.42 eV (EOM-CCSD); the CASPT2 value at the CASSCF geometry is very poor, 0.04 eV, but that obtained using the CCSD geometry is 0.21 eV.

In the previous calculations[32,33] of the properties of the triplet boat structure, the electronic state has been identified as $^3B_1$ (n,π^*). This identification was made as the potential-energy surface runs downhill from the $^3B_1$ C_{2v} transition state to the boat minimum,[32,33] while the $^3A_1$ (π,π^*) state appears to be a local minimum with respect to individual variations in θ and ϕ. This result is, however, contrary to the results of ESR studies,[26,27] which indicate that the boat structure is 80% (π,π^*) and 20% (n,π^*). Our calculations reveal that the $(\beta)^3A_1$ structure is also a transition state with respect to distortion in mode 16b, and further, this distortion also leads to the boat structure. Hence, the boat structure cannot be identified with just one of the C_{2v} states but rather must be considered a mixture of both, and we label this structure by the general label $^3A'$ appropriate for the C_s point group. Shown in Table 9 are the atomic Mulliken spin densities evaluated using B3LYP for all of the triplet states, as well as the observed values[26,27] in benzene crystal. The calculated values for $^3A'$ are in excellent agreement with experiment, but interestingly, the calculated values (at their C_{2v} minima) for $^3B_1$ and, to a lesser extent, $(\beta)^3A_1$, are similar; values for the other triplet states are quite different, however. Analyzing the nitrogen spin-density in terms of atomic s and p orbitals that rotate with the C_2-N-C_2 plane, the B3LYP results indicate 81% (π,π^*) character, in excellent agreement with the similarly deduced experimental result. Alternatively, analyzing the B3LYP results in terms of space-fixed crude-adiabatic functions indicates only 10% (π,π^*) character. Clearly, the interpretation of the nature of $^3A'$ depends on the method used. By examining the excitation coefficients and the nature of the molecular orbitals, it is clear that CASPT2, EOM-CCSD, TD-B3LYP, and TD-BLYP also indicate that $^3A_1$ is dominated by the adiabatically varying $(\beta)^3A_1$ (π,π^*) excitation.

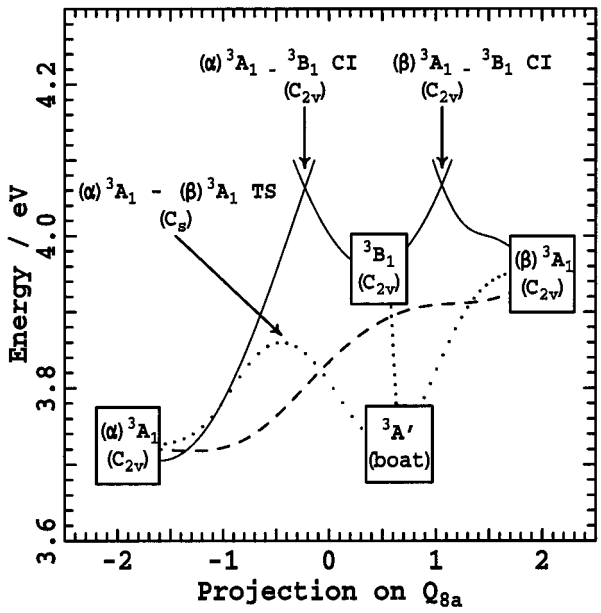

Figure 6. Map of the $^3A'$ hypersurface, shown as the CASPT2 energy versus the projection of the coordinates onto the ground-state dimensionless normal coordinate Q_{8a}, for linear interpolated motion between the various CCSD calculated stationary points.

3.4.2. Overview of the Lowest Triplet Hypersurface. Shown in Figure 6 is a map of the $^3A'$ surface obtained by evaluating the CASPT2 energy as a function of linear interpolations between the $(\alpha)^3A_1$, $(\beta)^3A_1$, $^3B_1$, and $^3A'$ CCSD structures. State-averaging over the three electronic configurations is employed in these calculations, as is C_s symmetry throughout, and the abscissa of the plot is the displacement from the ground-state geometry projected onto Q_{8a}. The approximate locations and energies of the $(\alpha)^3A_1-{}^3B_1$ and $(\beta)^3A_1-{}^3B_1$ conical intersections are apparent, and details are given in Table 5 and the Supporting Information. Starting at the $(\beta)^3A_1$ structure, the energy falls monotonically as the $^3A'$ boatlike minimum is approached. From $(\alpha)^3A_1$, which is a local minimum structure, the energy initially rises until a transition state is reached; although CASPT2 does not predict the occurrence of a transition state between $(\alpha)^3A_1$ and $(\beta)^3A_1$, at C_{2v} geometries, a barrier does indeed appear because of the implied b_1 distortion. From $^3B_1$, the energy initially falls slowly until the region of the $(\beta)^3A_1-{}^3B_1$ conical intersection is crossed, after which the dominant form of the wave function changes from (n,π^*) to (π,π^*) and the energy then falls rapidly toward that of $^3A'$.

3.4.3. Other Traps on the Triplet Surface. The other relatively low-lying triplet states of pyridine are $^3A_2$ (n,π^*) and $^3B_2$ (π,π^*). Table 7 shows that, like $^1A_2$, $^3A_2$ has a large symmetric-mode reorganization energy, and it is possible that this state forms the lowest-energy triplet state at some geometry and hence provides another trap for triplet excitation. However, the predicted energy differences at the C_{2v}-optimized geometries from Table 8 all indicate that $^3A_2$ lies 0.3−0.6 eV above $^3B_1$. Further, the antisymmetric-mode relaxation energies for $^3A_2$ shown in Table 7 indicate the likelihood of only a mild in-plane distortion, and hence, its minimum should remain well above the $^3A'$ surface. In Table 10 are given the calculated vertical absorption energies evaluated at the C_{2v}-optimized structures of $(\alpha)^3A_1$, $(\beta)^3A_1$, $^3B_1$, $^3A_2$, and $^3B_2$. Clearly, the first there states are the lowest-energy ones at their respective C_{2v}-optimized geometries, while $(\alpha)^3A_1$ clearly lies well below $^3B_2$.

TABLE 10: Calculated Vertical Energies Differences, in eV, between Various Triplet States of Pyridine Obtained at C_{2v}-)ptimized Geometries[a]

	$(\alpha)^3A_1 \rightarrow$				$(\beta)^3A_1 \rightarrow$				$^3B_1 \rightarrow$				$^3A_2 \rightarrow$				$^3B_2 \rightarrow$			
method	(β) $^3A_1$	$^3B_1$	$^3A_2$	$^3B_2$	(α) $^3A_1$	$^3B_1$	$^3A_2$	$^3B_2$	(α) $^3A_1$	(β) $^3A_1$	$^3A_2$	$^3B_2$	(α) $^3A_1$	(β) $^3A_1$	$^3B_1$	$^3B_2$	(α) $^3A_1$	(β) $^3A_1$	$^3A_2$	$^3B_1$
CCSD	2.00	1.54	1.68	1.53	1.56	0.63	2.68	1.32	1.07	0.55	1.28	1.39	−0.22	1.26	−0.01	1.36	−0.46	−0.19	1.34	0.10
EOM-CCSD	2.24	1.63	1.78	1.44	1.88	0.90	2.85	1.34	1.36	0.16	1.26	1.24	−0.37	1.45	−0.01	1.00	−0.76	0.35	1.48	0.24
CASSCF(8,11)	2.08	2.08	2.63	1.53	1.63	1.17	3.19	1.37	0.96	−0.34	1.52	0.85	−1.20	1.38	−0.35	0.21	−0.96	0.22	1.76	0.38
CASPT2[b]	1.74	1.12	1.29	0.93	1.22	0.42	1.94	0.75	1.22	0.41	1.10	1.06	0.05	1.27	−0.04	0.88	−0.47	0.21	1.06	0.11
CIS	2.47	2.34	3.49	1.69	2.49[c]	1.95[c]	4.94[c]	1.90[c]	1.15	−0.62	2.70	0.99	−2.12	0.70	−0.31	−0.83	−1.18	0.45	2.87	0.72
TD-B3LYP	2.20	1.32	1.38	1.30	1.92	0.56	2.44	1.23	1.60	0.48	1.16	1.39	−0.11	1.71	0.09	1.19	−0.59	0.43	1.05	−0.03
TD-BLYP	1.89	0.81	0.62	0.97	1.53	0.03	1.48	0.81	1.70	0.94	0.78	1.49	0.64	2.19	0.31	1.65	−0.21	0.45	0.64	−0.16
B3LYP	2.09	1.20	1.13	1.17	1.54	0.36	2.15	0.94	1.27	0.84	1.07	1.37	1.55	3.91	0.18	0.00	−0.12	0.18	1.17	0.11
BLYP	1.91	0.99	0.85	1.02	1.35	0.30	1.83	0.76	1.18	0.88	0.85	1.27	1.33	5.09	0.62	3.55	−0.05	0.22	0.98	0.10

[a] Evaluated using the cc-pVDZ basis set. [b] At the CASSCF(8,11)-optimized geometry. [c] At the CCSD-optimized geometry.

TABLE 11: Magnitude of the Discontinuity in CASSCF-Based Potential-Energy Surfaces, in eV

method	$^1B_1$ (n,π^*)	$^1A_2$ (n,π^*)	$^3B_1$ (n,π^*)	$^3A_1$ (π,π^*)	$(2)^3A_1$ (π,π^*)
CASSCF(8,11)	−0.47	−0.05	−0.56	−0.037	−0.10
CASPT2(8,11)	0.10	0.01	0.49	−0.093	0.02
CASSCF(8,7)	−0.35		−0.032	0	

However, while TD-BLYP, B3LYP, and BYLP all predict that $^3A_2$ is the lowest-energy triplet state at its own equilibrium structure, TD-B3LYP and CASPT2 predict that $(\alpha)^3A_1$ is close in energy, and CCSD and EOM-CCSD predict $(\alpha)^3A_1$ to be significantly lower. Hence, it is possible that $^3A_2$ does form a trap in the triplet manifold, albeit one of relatively high yet accessible energy.

3.4.4. The Boat Structure of $^1B_1$. The structure of $^1B_1$ is known from spectroscopic data[21] to be quasi-planar (i.e., to have a nonplanar distorted structure for which the distortion energy is less than the zero-point energy), with a very small antisymmetric-mode (ν_{16b}) reorganization energy of just 4 cm^{-1} or 0.001 eV. Chachisvilis and Zewail[2] have shown that it is necessary to include this distortion in models of the photophysics of pyridine, and our highest-quality methods, EOM-CCSD and CASPT2, both predict a large distortion similar to that predicted for $^3B_1$ (see Table 6) but with a much smaller reorganization energy. Qualitatively, the differing behavior of $^1B_1$ and $^3B_1$ is attributed to the differing energy gaps to the vibronically coupled $^1A_1$ and $^3A_1$ states: $^3A_1$ is nearby, the mixing is very strong, and the bond lengths (see Table 5) and other properties are intermediary between those of $^3B_1$ and $^3A_1$, whereas $^1A_1$ is very distant, so that the mixing is weak and the bond lengths and other properties strongly reflect those of $^1B_1$ alone.

Earlier computations by Chachisvilis and Zewail[2] at the CIS and TD-B3LYP levels also support the existence of a boat distortion, with CIS geometry optimization predicting a distorted structure,[34] while TD-B3LYP single-point energy calculations confirmed that the distorted structure has lower energy. However, we have optimized the geometry of $^1B_1$ using TD-B3LYP and find that the C_{2v} structure is, in fact, a local minimum, and hence, this method does not predict the observed distortion. Also, although CIS predicts distortion for $^1B_1$, it is the only method used that *fails* to predict distortion for $^3B_1$, for which the reorganization energy should be several orders of magnitude *larger*. Hence, the CIS results for the two states are erratic, whereas the density-functional results indicate systematic underestimation of the driving force for symmetry lowering; this lower driving force is consistent with the observation from Table 3 that the density-functional methods appear to significantly underestimate the energy of the B_1 (n,π^*) states and hence show less vibronic coupling with the A_1 (π,π^*) states.

CASSCF vibrational frequency calculations[9] at C_{2v} symmetry have also been used to study the boat distortion, but as no imaginary b_1 frequencies were obtained, it was concluded that this distortion did not occur. However, it is shown in Table 11 that the CASSCF potential-energy surfaces produced using both our active space and that used in the earlier calculations is unstable to symmetry lowering, and hence, their conclusion is invalid. Broken-symmetry CASSCF calculations do indeed predict a distortion. However, this approach is unreliable, as it predicts a realistic antisymmetric-mode reorganization energy for $^1B_1$ but fails to reproduce the extensive additional stabilization for $^3B_1$. Further, the optimized geometry for $^3B_1$ is very poor, with $\alpha = 2.3°$ rather than ca. 40°.

For $^1B_1$ (S_1), the rotational constants *A*, *B*, and *C* have been determined from high-resolution spectroscopy[9] and, in principle, can be used to verify proposed structures for this state. They are given in Table 12, along with the values calculated at C_{2v}- and C_s-optimized geometries. Although calculated rotational constants should be averaged over the zero-point motion before comparison with experiment, it is clear from the table that *both* the C_{2v} and C_s structures are consistent with the experimental data, and so, such averaging is not necessary.

3.5. Excited-State Vibration Frequencies. The vibrational frequencies of the excited states have been evaluated using a variety of methods, and full results including the normal modes, Duschinsky rotation matrices, and normal-mode projected displacements from the ground state are given in full in the

TABLE 12: Calculated Rotational Constants *A*, *B*, and *C*, in cm^{-1}, for the S_1 (n-π^*) State of Pyridine[a]

	A		*B*		*C*	
method	C_{2v}	C_s	C_{2v}	C_s	C_{2v}	C_s
EOM-CCSD	0.20256	0.20404	0.18289	0.18282	0.09611	0.097606
CASSCF(8/11)	0.20517	0.20728	0.18274	0.18155	0.09665	0.09872
CIS	0.20881	0.20941	0.18639	0.18774	0.09848	0.10033
TD-B3LYP	0.20367	−	0.18469	−	0.09686	−
TD-BLYP	0.19957	−	0.18342	−	0.09558	−
exp.[b]	0.202 7(67)		0.182 7(43)		0.095 5(8)	

[a] All results obtained using the cc-pVDZ basis set, at either the C_{2v}- or C_s- (boatlike) optimized geometry. [b] From ref 9.

TABLE 13: Comparison of Observed and Analytically Calculated (Unscaled) Frequencies, in cm^{-1}, for the S_1 $^1B_1$ (n,π^*) Excited State of Pyridine[a]

mode	type	symm.	obs.[b]	EOM-CCSD	CASSCF(8/11)	CIS	CASSCF(8/7)/ 6-31G**[c]	CIS/ 6-31G*[d]	CIS/ 3-21G[d]
12	$C_{\|\|}$	a_1	997	984	990	977	988		
6a	$C_{\|\|}$	a_1	542	562	590	604	594	609	630
11	$H_\perp$	b_1	484	589	544	678	545		
16b	$C_\perp$	b_1	58	**134i**	87	**202i**	80	**214i**	74
10a	$H_\perp$	a_2	331	494	820	526	562		
16a	$C_\perp$	a_2	326	327	472	448	428	453	476
RMS error				122	211	164	109	178	101

[a] All calculations are performed using the cc-pVDZ basis set. The vibration types, mapped by examination of the Duschinsky matrix elements, are: $C_{\|}$, in-plane ring bend; $H_\perp$, out-of-plane hydrogen bend; $C_\perp$, out-of-plane ring bend; see ref 3 for details. [b] See ref 1. [c] See ref 9. [d] See ref 34.

TABLE 14: Comparison of Observed and Analytically Calculated (Unscaled) Frequencies, in cm^{-1}, for the S_2 $^1B_2$ (π,π^*) Excited State of Pyridine[a]

mode	type	symm.	obs.[b]	EOM-CCSD	CASSCF (8/11)	CIS	CASSCF (8/7)[c]
9a	$H_{\|\|}$	a_1	1215	1157	1148	1191	1278
1	CC	a_1	950	956	969	949	978
6a	$C_{\|\|}$	a_1	550	520	558	564	565
16a	$C_\perp$	a_2	327	378	327	389	299
RMS error				42	35	34	38

[a] All calculations are performed using the cc-pVDZ basis set. The vibration types, mapped by examination of the Duschinsky matrix elements, are: $C_{\|}$, in-plane ring bend; $H_\perp$, out-of-plane hydrogen bend; $C_\perp$, out-of-plane ring bend; see ref 3 for details. [b] See refs 1 and 14. [c] See ref 9.

Supporting Information. In Tables 13 and 14 are shown the observed vibration frequencies for $^1B_1$ (S_1) and $^1B_2$ (S_2), respectively, as well as the corresponding calculated frequencies, while Table 15 shows the calculated frequencies for some key modes for the various stationary points of the $^3A'$ surface. For each calculated normal mode of imaginary frequency, Table 16 shows the well depth, well-bottom harmonic frequency, and the effective frequency (i.e., the $0 \rightarrow 1$ transition energy) obtained by evaluating the energy as a function of the displacement of the normal mode. For comparison, Table 16 also shows the available experimental data. Note that the zero-point energy changes given previously in Table 4 were evaluated using these anharmonic values for the double-well modes.

In general, all of the computational methods used for the singlet states (EOM-CCSD, CASSCF, and CIS) produce useful results, with those from EOM-CCSD being clearly superior. The most significant errors predicted using it are for ν_{10a} of $^1B_1$ (S_1), 494 cm^{-1} (obs. 331), and the modes with double-well potentials, ν_{16b} of $^1B_1$, 98 cm^{-1} (obs. 58), and ν_{10a} of $^1B_2$, 201 cm^{-1} (obs. 327). The result for ν_{16b} is somewhat flattering, however, as the well depth increases from 32 to 138 cm^{-1} upon full relaxation (see Table 7), much larger than the observed value[21] of 4 cm^{-1}. All methods predict the observed[1] large Duschinsky rotation of modes 10a and 16a of $^1B_1$; many other Duschinsky rotations and mode-order inversions are predicted, and these are detailed in the Supporting Information.

4. Simulations of the Observed Spectra

Using the results of section 3, the harmonic approximation to the ground- and excited-state potential-energy surfaces, and the Condon approximation (that the transition moment is coordinate-independent), we have simulated the observed absorption and emission spectra of pyridine. Note that Duschinsky rotation effects are *fully* included in these calculations but usually do not have a significant influence on the calculated band contours. When required, we have also considered non-Condon effects, and, for the triplet states, introduced a large vibronic coupling model to simulate both the low-resolution and high-resolution spectra. Duschinsky effects, other than those involving the vibronically active modes, are ignored in these vibronic coupling calculations, however. In all cases, the calculated spectra are shifted so that its origin matches the observed origin, and total intensities are normalized.

4.1. The Singlet States. In Figure 3 are shown the spectra obtained using the CCSD force field for the ground state and the EOM-CCSD force fields for $^1B_1$ (S_1) and $^1B_2$ (S_2), as well as the observed[15] absorption and fluorescence excitation spectra. The force fields used were those evaluated at C_{2v} symmetry,

TABLE 15: Some Calculated Vibration Frequencies, in cm^{-1}, for Pyridine Excited States[a]

state	method	ν_1	ν_5	ν_{6a}	ν_{8a}	ν_{8b}	ν_{9a}	ν_{10a}	ν_{11}	ν_{12}	ν_{16a}	ν_{16b}
(α)$^3A_1$	CCSD	920		576	1527		1220			1004		
	CASSCF(8/11)	960	962	602	1550	1882	1236	485	476	1069	143	287
	CIS	609	980	1118	1586	**613i**	975	665	508	1095	195	376
	B3LYP	1088	959	911	1497	633	911	304	393	579	**261i**	335
	BLYP	563	929	877	1442	614	877	**753i**	362	563	160	319
(β)$^3A_1$	CCSD	928		542	1718		1219			1015		
	CASSCF(8/11)	959	**146i**	573	1540	**222i**	1185	714	472	1081	372	159
	B3LYP	743	961	923	1705	**1070i**	1209	712	**1013i**	743	372	**87i**
	BLYP	532	911	891	1632	**1005i**	1175	675	2057	724	350	**100i**
$^3B_1$ (C_{2v})	CCSD	983		562	1620		1172			1016		
	CASSCF(8/11)	1018	857	598	1704	1611	1241	565	**1531i**	1088	446	393
	CIS	1087	1079	605	1742	1605	1247	327	749	1070	469	329
	B3LYP	568	861	981	1581	939	1159	385	413	923	452	**434i**
	BLYP	555	797	966	1514	863	1128	**295i**	**558i**	895	426	309
$^3A'$ (C_s)	CCSD	844	904	505	1541	1339	1164	888	557	1003	378	303
	B3LYP	935	907	1003	1500	1332	1150	890	588	848	445	298
	BLYP	504	866	969	1439	1268	1120	851	572	929	409	276

[a] Mode assignments are made by examination of the Duschinsky matrix elements.

TABLE 16: Properties and Anharmonic Vibrational Analysis of All Double-Well Potentials, in cm^{-1}

state	mode	symm.	method	harm.	anharm.	well depth
$^1B_1$	16b	b_1	EOM-CCSD	129	98	32
	16b	b_1	CIS	202	69	109
	16b	b_1	CASSCF(8/11)	162	82	59
	16b	b_1	obs[a]		58	4
	8b	b_2	EOM-CCSD	734	898	25
$^1A_2$	19b	b_2	EOM-CCSD	795	831	77
	8b	b_2	CASSCF(8,11)	1559	614	570
$^1B_2$	10a	a_2	EOM-CCSD	260	201	57
	10a	a_2	CIS	487	284	309
$(\alpha)^3A_1$	8b	b_2	CIS	552	606	56
	16a	a_2	B3LYP	232	238	35
	10a	a_2	BLYP	594	215	284
$(\beta)^3A_1$	8b	b_2	EOM-CCSD[b]	202	206	0
	8b	b_2	CASSCF(8,11)	768	350	230
	8b	b_2	B3LYP	151	454	2
	8b	b_2	BLYP	515	325	125
	11	b_1	EOM-CCSD[b]	361	149	113
	5	b_1	CASSCF(8,11)	121	397	1
	11	b_1	B3LYP	505	33	500
	16b	b_1	BLYP	109	276	35
$^3B_1$	16b	b_1	B3LYP	377	2	721
	11	b_1	BLYP	408	19	524
	11	b_1	CASSCF(8/11)	525	14	722
	10a	a_2	BLYP	231	409	10
$^3A_2$	8b	b_2	EOM-CCSD	2354	629	900
	8b	b_2	TD-B3LYP[b]	1514	606	530
	8b	b_2	TD-BLYP[c]	833	1204	60
	10a	a_2	TD-B3LYP[b]	1654	1477	0
$^3B_2$	16b	b_1	B3LYP	57	135	2
	11	b_1	BLYP	74	239	1
	16b	b_1	BLYP	55	141	1

[a] From ref 21. [b] Using B3LYP normal mode. [c] Using BLYP normal mode.

allowing for the inclusion of full anharmonic treatments (see Table 16) for modes of imaginary frequency. For $^1B_1$, the calculated spectrum is in reasonable agreement with the observed fluorescence excitation spectrum, the observed spectrum showing additional intensity near the origin due to the effects of vibronic coupling in the a_2 and b_1 modes,[1] as well as possibly some additional intensity at high frequency due to emission from $^1B_2$. Similarly, the calculated absorption spectrum for $^1B_2$ is in reasonable agreement with the observed one, which shows additional intensity at low frequency due to the absorption of $^1B_1$.

The observed fluorescence spectrum[17] of pyridine is shown in Figure 7 as curve F, along with various spectra calculated using the EOM-CCSD force field for the emitting state, $^1B_1$. Curve A shows the calculated spectrum obtained from the force field of C_{2v} symmetry. This simulation also includes explicit provision for the shallow double well in ν_{16b} described in Table 16, but this effect has only minor consequences. The emission is clearly calculated to occur significantly too high in frequency, and this is reflected in the difference between the observed and calculated ground-state reorganization energies λ_G; for brevity, these quantities are not tabulated, but they can be obtained from the adiabatic energy differences shown in Table 8 and the vertical emission energies shown in Table 17. The observed value is obtained by extrapolating the spectrum to low frequency and applying eq 1, which gives $\lambda_G = 0.7$ eV, whereas the calculated values are all much smaller, 0.4 eV $< \lambda_G <$ 0.55 eV.

Alternatively, curve C in Figure 7 shows the spectrum calculated using the EOM-CCSD harmonic force field for the C_s-optimized structure of $^1B_1$. This spectrum is shifted far too

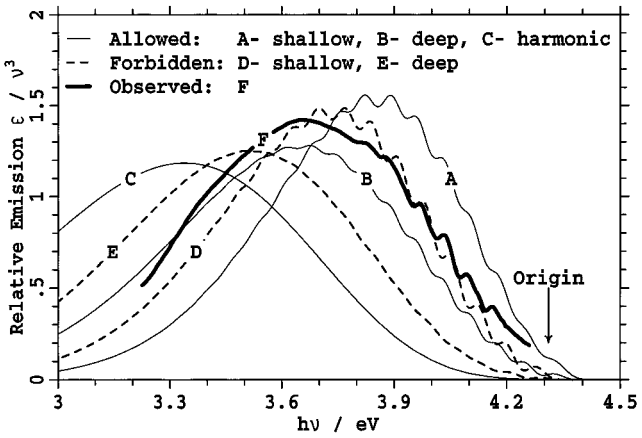

Figure 7. The observed fluorescence spectrum[17] of pyridine is compared to calculated spectra, normalized to constant area, for the electronically allowed and b_1 vibronically induced intensity, assuming either a harmonic potential about the C_s (boatlike) minimum, or shallow or deep anharmonic double well potentials.

low in energy, a consequence of the very high ground-state antisymmetric-mode reorganization energies, which, from the data given in Table 17, are calculated to range from 0.5 to 0.9 eV. A calculated spectrum that is comparable to the observed one is shown as curve B, obtained using a deep double well in ν_{16b} indicative of the actual anharmonic EOM-CCSD excited-state potential (see Table 7). This well is sufficiently deep to support localized zero-point vibration, which, unfortunately, is contrary to observation,[21] and hence this effect cannot be used to explain the observed fluorescence.

A significant fraction of the intensity of the absorption to $^1B_1$ arises because of vibronic coupling in ν_{10a} and ν_{16b}. For emission, the vibronic coupling through ν_{16b} will be most significant because of the double-well potential in this mode. Curve D in Figure 7 shows the emission expected due purely to vibronic coupling in ν_{16b} using the (realistic) shallow double-well potential. We do not attempt to scale the contributions of the allowed intensity (curve A) and the vibronic intensity (curve D), as this would require precise knowledge of the (small) allowed transition moment and the vibronic coupling constant, but by inspection, approximately equal contributions would lead to a spectrum that is close to that observed. Curve E shows the vibronically allowed emission obtained using the deep double well, and this is clearly shifted too low in energy. We thus conclude that the observed fluorescence band contour is dominated by both the fine details of the double-well potential in ν_{16b} and the ratio of the allowed to the forbidden intensity.

4.2. Model for the Triplet States. The triplet states have been observed through low-resolution[22] and high-resolution[21] singlet-to-triplet absorption, phosphorescence,[24] and electron energy-loss spectroscopy.[20] Interpretation of the high-resolution absorption spectrum requires a vibrational analysis to be performed on the very complex $^3A'$ surface depicted in Figure 6, as well as an understanding of the spin−orbit coupling effects that provide the transition intensity. We start by developing models for both.

4.2.1. Vibronic Coupling. We use a mixed vibronic−electronic coupling model expanded in terms of the diabatic states $(\alpha)^3A_1$ and $(\beta)^3A_1$ and the crude-adiabatic state $^3B_1$. Four totally symmetric modes, 6a, 1, 9a, and 8a, as well as two b_1 modes, 16b and 11, are included explicitly in the simulations, and the values of all of the parameters used are given in Table 19. The vibrational modes are characterized by their frequency ν_i and displacement δ_i in each state, where the displacements

TABLE 17: Calculated Vertical Emission Energies, E_{VE}, in eV, for Pyridine[a]

		$^1B_1$ (n,π^*)		$^1A_2$ (n,π^*)		$^1B_2$ (π,π^*)	(α)$^3A_1$ (π,π^*)		(β)$^3A_1$ (π,π^*)	$^3B_1$ (n,π^*)	$^3A'$ (mixed)	$^3A_2$ (n,π^*)		$^3B_2$ (π,π^*)
method	basis set	C_{2v}	C_s	C_{2v}	C_s	C_{2v}	C_{2v}	C_s/C_2	C_{2v}	C_{2v}	C_s	C_{2v}	C_s	C_{2v}
CCSD	cc-pVDZ						3.17		3.28	3.49	2.05	3.84		4.52
CCSD	aug-cc-pVDZ						3.15			3.47	2.04			4.43
CCSD(T)[b]	cc-pVDZ						3.38			3.62	2.26			4.58
CCSD(T)[b]	aug-cc-pVDZ						3.37			3.59	2.25			4.36
EOM-CCSD	cc-pVDZ	4.28	3.74	3.98	3.90	4.92	3.15	3.13[g]	3.26	3.65	2.12	3.92	3.64	4.49
CASSCF(8,11)	cc-pVDZ	4.57	3.40	4.80	4.62	4.72	3.19		3.37	4.16		4.76		4.68
CASPT2[c]	cc-pVDZ	3.97	3.16	3.71	3.63	4.45	3.34		3.52	3.47		3.66		4.24
CASPT2[c]	aug-cc-pVDZ	3.95	3.09			4.46	3.22			3.42				4.16
CASPT2[b]	cc-pVDZ	3.98	3.50			4.40	3.18			3.41	2.16	3.59	3.39	4.12
CASPT2[b]	aug-cc-pVDZ	3.89	3.42			4.43	3.13			3.36	2.12			3.94
CIS	cc-pVDZ	4.86	4.23	5.26		6.06	2.86	2.71[h]	2.61	3.91	2.86	5.04		4.49
TD-B3LYP	cc-pVDZ	3.95	[3.95][i]	3.60	3.54	5.22	2.93	2.87[h]	3.02	3.20	1.95[d]	3.48	3.14	4.14
TD-BLYP	cc-pVDZ	3.55	[3.55][i]	3.07		4.95	3.15	3.03[h]	3.28	2.94	2.00	2.98	2.83	3.97
B3LYP	cc-pVDZ						3.25	3.19[h]	3.44	3.37	2.23	3.52	3.18	4.25
BLYP	cc-pVDZ						3.28	3.16[h]	3.50	3.35	2.34	3.33	3.18	4.14
Obs.- raw	-	3.6[e]									2.66[f]			
Obs. + ZPE corr.	-	3.76									2.84			

[a] Evaluated at the individually optimized excited-state geometries. [b] At the CCSD- or EOM-CCSD-optimized geometry. [c] At the CASSCF(8,11)-optimized geometry. [d] At the TD-BLYP-optimized geometry. [e] Our analysis (see text) of fluorescence spectrum.[17] [f] Our analysis and assignment of the observed phosphorescence spectrum.[24] [g] C_s. [h] C_2. [i] The equilibrium geometry is actually of C_{2v} symmetry.

TABLE 18: CASSCF(8,6) Calculated Spin−Orbit Coupling Constants between Adiabatic States, in cm^{-1} [a]

states	$^1A_1$ (S_0) $E = 0$ $f = 0$	$^1B_1$ (S_1) $E = 4.9$ $f = 0.003$	$^1B_2$ (S_2) $E = 5.1$ $f = 0.029$	$^1A_2$ $E = 5.5$ $f = 0$	(2)$^1A_1$ $E = 6.4$[b] $f = 0.09$	(2)$^1B_1$ $E = 9.0$[b] $f = \sim 0$	(3)$^1A_1$ $E = 7.2$ $f = 0.45$	(2)$^1B_2$ $E = 7.2$ $f = 0.45$
$^3A_1$	0	13.9	1.6	1.7	0	24.5	0	0.0
(2)$^3A_1$	32.6	−16.6	−0.4	1.1	0	14.9	0	0.4
$^3B_1$	30.3	0	1.5	1.1	3.6	0	1.2	1.3

[a] At the ground-state B3LYP/cc-pVDZ geometry. E are observed vertical excitation energies, in eV, while f are observed[14] allowed oscillator strengths. [b] CASPT2 value.

TABLE 19: Parameters Used in the Spectral Model for the Triplet States[a]

	frequency ν_i/cm^{-1}				displacement δ_i			vibronic coup.[b] α_i^x/cm^{-1}	
mode i	S_0	(α)$^3A_1$	(β)$^3A_1$	$^3B_1$	(α)$^3A_1$	(β)$^3A_1$	$^3B_1$	(α)$^3A_1$−$^3B_1$	(β)$^3A_1$−$^3B_1$
6a	607	576	542	505	−0.89	0.29	2.2	0	0
1	1014	920	928	844	1.15	1.20	−1.2	0	0
9a	1247	1220	1219	1164	0.91	−1.41	−1.1	0	0
8a	1669	1527	1718	1541	−2.2	2.3	0.47	0	0
16b	412	412	412	303	0	0	0	800	−1200
11	712	712	712	557	0	0	0	−1000	1400

[a] Other parameters are the energy zero $E_0 = 29\,900$ cm^{-1}, the energy spacings $\Delta E_{\alpha\beta} = 2100$ cm^{-1} and $\Delta E_{\alpha n} = 2600$ cm^{-1}, the allowed electronic coupling $J_{\alpha\beta} = 2700$, and the transition-moment ratio $\mu_\alpha/\mu_\beta = 7.7/18.1$. [b] Note that vibronic coupling constants are often defined as $2^{-1/2}\alpha_i^x$, see text.

are relative to the ground-state geometry and are expressed in terms of ground-state dimensionless normal coordinates. In most cases, the values used for these parameters were obtained from the CCSD normal coordinate analyses in C_{2v} symmetry for the S_0, (α)$^3A_1$, (β)$^3A_1$, and $^3B_1$ states, full results for which are given in Supporting Information. Note that Duschinsky rotation effects involving other vibrational modes or electronic states are not included in these calculations. The frequencies for the b_1 modes of (α)$^3A_1$ and (β)$^3A_1$ were set simply to the ground-state values, whereas those for $^3B_1$ were taken from the CCSD force field in C_s symmetry. The displacements in the dominant mode 8a in states (α)$^3A_1$ and (β)$^3A_1$ were empirically adjusted from their calculated values of −1.91 and 1.99, respectively, to values of −2.2 and 2.3, respectively, to obtain a qualitatively correct description of the observed high-resolution singlet-to-triplet absorption spectrum.

In this model, the two diabatic states (α)$^3A_1$ and (β)$^3A_1$ interact through an allowed electronic coupling $J_{\alpha\beta}$, the value of which (2700 cm^{-1}) is determined empirically in order to fit the calculated TD-B3LYP, EOM-CCSD, and CASPT2 adiabatic surfaces for (α)$^3A_1$ and (β)$^3A_1$; the calculated and fitted surfaces are shown in Figure 4, and there does appear to be considerable scope for variation of this parameter. The remaining parameters needed to define the (α)$^3A_1$−(β)$^3A_1$ part of the surface are the absolute energy, E_0, of the minimum of the (α)$^3A_1$ well, which is adjusted to fit the origin of the observed high-resolution spectrum, and the energy difference between the well minima, $\Delta E_{\alpha\beta}$, which is set at 2100 cm^{-1} in order to obtain the correct qualitative description of the spectrum. The final diabatic surfaces, and the resulting adiabatic ones produced by diagonalizing the resultant electronic Hamiltonian, are shown in Figure 4. From this figure it is clear that the model diabatic surfaces are very similar to the CCSD surfaces upon which they are based. However, whereas the model lower adiabatic surface shows a clear transition state separating the (α)$^3A_1$ and (β)$^3A_1$ minima, this transition state is suppressed in the EOM-CCSD and CASPT2 results. Clearly, the appearance or not of a transition state is quite sensitive to small changes in the

calculated potential parameters but, in terms of our forthcoming analysis of the high-resolution spectrum, is an essential feature. TD-B3LYP predicts a small barrier, with the shape of this surface being approximately the average of those for the fitted and the CASPT2/EOM-CCSD surfaces.

We expand the components of the vibrational wave functions for modes 16b and 11 at the C_s minimum of the $^3A'$ surface in terms of harmonic-oscillator functions centered around a structure of C_{2v} symmetry. As the (dimensionless) normal-mode projections of this minimum onto these two modes are 4.9 and −3.3, respectively (see Supporting Information), and as the antisymmetric relaxation energies are quite large so that a significant number of bound levels occur below the barrier of the double-minimum potential, such an expansion appears ill-devised, requiring the use of a very large number of vibrational basis functions in order to describe correctly the low-lying vibrational levels. This representation is used because it leads to the ready formulation of the electronic Hamiltonian between the three interacting states

$$\mathbf{H} = \begin{bmatrix} E_0 + \sum_i \frac{k_i^\alpha}{2}(Q_i - \delta_i^\alpha)^2 & J_{\alpha\beta} & \sum_i \alpha_i^\alpha Q_i \\ J_{\alpha\beta} & E_0 + E_{\alpha\beta} + \sum_i \frac{k_i^\beta}{2}(Q_i - \delta_i^\beta)^2 & \sum_i \alpha_i^\beta Q_i \\ \sum_i \alpha_i^\alpha Q_i & \sum_i \alpha_i^\beta Q_i & E_0 + E_{\alpha n} + \sum_i \frac{k_i^n}{2}(Q_i - \delta_i^n)^2 \end{bmatrix} \quad (3)$$

where the effective force constants for state x [$\alpha \equiv (\alpha)^3A_1$, $\beta \equiv (\beta)^3A_1$, $n \equiv {}^3B_1$] are given by

$$k_i^x = hc\frac{(\nu_i^x)^2}{\nu_i^{GS}} \quad (4)$$

where GS is the ground state, for which the dimensionless normal coordinates Q_i are defined, and α_i^x are vibronic coupling constants[56] for the interaction of $^3B_1$ with state x through vibration i. Note that, in the spectroscopic literature, vibronic coupling constants have traditionally been defined as $\alpha_i^x\langle 0|Q_i|1\rangle = 2^{-1/2}\,\alpha_i^x$ where $\langle 0|Q_i|1\rangle$ is a harmonic-oscillator vibrational integral,[57] contrary to the more general usage adopted here.

4.2.2. Values of the Vibronic Coupling Constants. To estimate the vibronic coupling constants, we first employed direct CASSCF calculations. This, however, was unsuccessful, as the CASSCF potential-energy surface depicts only minor distortions in the b_1 modes (see Table 7) and hence greatly underestimates the coupling constants. Next, we used CNDO/S to evaluate them from the coordinate dependence of the calculated $(\alpha)^3A_1$- and $(\beta)^3A_1$-to-$^3B_1$ triplet-to-triplet transition moment. Similar approaches for singlet states[56,58,59] have been shown to produce qualitatively descriptive results; we obtained 558 and −1491 cm^{-1} for the interaction with $(\alpha)^3A_1$ via modes 16b and 11, respectively, and −1075 and 475 cm^{-1} for those with $(\beta)^3A_1$. However, we were unable to interpret the observed spectra using these parameters.

For the simple scenario in which one vibrational mode couples two electronic states, values of the vibronic coupling constant can be obtained directly from calculated displacement to the C_s minimum using[55] $\alpha_i = \delta_i\nu_i$. This approach has the interesting property that it can be applied to any electronic structure method, but it is not applicable here as two electronic states and two vibrational modes are involved. We have generalized this procedure, however, by applying the Born−Oppenheimer approximation directly to the model Hamiltonian, eq 3, fitting the vibronic coupling constants and the energy gap parameter $\Delta E_{\alpha n}$ so that the primary features (antisymmetric displacements and reorganization energies) of the model Hamiltonian match those calculated using CCSD. Two different solutions were found by this process, the one shown in Table 19 being the solution that depicted the strongest coupling as arising between $(\beta)^3A_1$ and $^3B_1$ rather than between $(\alpha)^3A_1$ and $^3B_1$. Three of the four values agree to within 30% to the CNDO/S ones; however, the coupling to $(\beta)^3A_1$ through ν_{11} is markedly different. Note that the largest values are typical of strong vibronic coupling in aza-aromatics.[60]

4.2.3. Spin−Orbit Coupling. CASSCF(8,6) spin−orbit coupling calculations were performed at the ground-state equilibrium geometry, and the results are shown in Table 18. The strongest couplings are predicted to occur between $^3B_1$, $(2)^3A_1$, and the ground state, allowing the observed rapid nonradiative decay and poor phosphorescence quantum yields[1,2,24] to be understood. In magnitude, the next largest couplings are predicted between the $^3A_1$ states and $(2)^1B_1$, but, as shown in Table 18, this singlet state is both very weakly allowed and quite distant in energy and so is unlikely to contribute to the observed singlet-to-triplet absorption. The only other strong couplings occur between the $^3A_1$ states and $^1B_1$ (S_1); although $^1B_1$ is very close in energy, it is also rather weakly allowed. Coupling to the intense but distant $(2)^1B_2$ state provides another option, but the calculated spin−orbit coupling strength is rather weak. Quantitatively, the oscillator strength f_T of a triplet state stealing intensity from a singlet state of oscillator strength f_S can be expressed as

$$f_T = f_S\left(\frac{\alpha_{S,T}^{SO}}{\Delta E_{S,T}}\right)^2 \quad (5)$$

where $\alpha_{S,T}^{SO}$ is the spin−orbit coupling constant and $\Delta E_{S,T}$ is the state energy gap, which is assumed to be large in comparison to the spectral bandwidths. Crudely, taking the energies of both $(\alpha)^3A_1$ and $(\beta)^3A_1$ at vertical excitation to be 4.1 eV and ignoring all interference effects, the ratios of intensity entering the $^3A_1$ system from $^1B_2$ and $(2)^1B_2$ to that from $^1B_1$ are 3% and 4%, respectively. Compared to $^3A_1$, the relative intensity stolen by $^3B_1$ (assuming a vertical energy of 4.4 eV) is 6% from $^1B_2$, 13% from $(2)^1A_1$, and 4% from each $(3)^1A_1$ and $(2)^1B_2$. These ratios are quite suggestive, and thus we assume that, in the gas phase, the $^3A'$ system is intensified only through spin−orbit coupling of the $^3A_1$ states with $^1B_1$.

The above spin−orbit coupling constants are evaluated for diabatic states, but for use with eq 4, they are actually required with respect to the basis *diabatic* states. Initially, we assume that these are proportional to the spin−orbit couplings between $(\alpha)^3A_1$ and $(\beta)^3A_1$ with $^3B_1$, and that these are independent of nuclear displacement. Table 18, however, shows spin−orbit couplings calculated at the ground-state geometry for the interactions between *adiabatic* states. To obtain the required parameters, we initially transformed to results given in this table using the diabatic-state mixings depicted in Table 1. However,

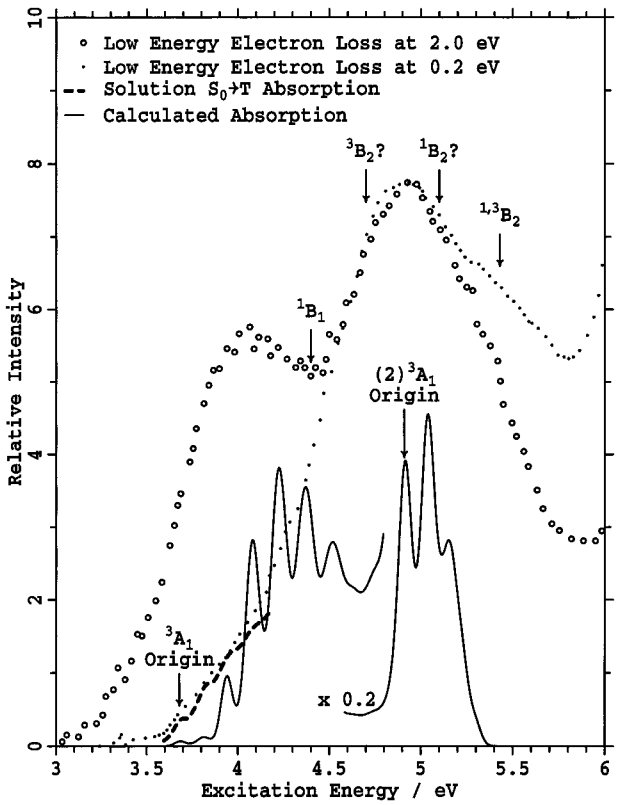

Figure 8. The observed low-energy electron-loss spectra[20] at 0.2 and 2.0 eV and the observed singlet-to-triplet absorption[22] in 4-trimethylpentane solution in the presence of dissolved O_2 are compared with the absorption spectrum calculated from the vibronic coupling model (including only a_1 modes) for the $^3A_1$ and $(2)^3A_1$ states of pyridine. Suggested assignments for other states (see Table 3) are also indicated.

the results were too variable with the initial geometry, an effect that, like the failure of the fitted diabatic surface to reproduce the EOM-CCSD and CASPT2 adiabatic profiles shown in Figure 4, is indicative of the complexity of the interaction and the simplicity of our model. Nevertheless, we obtained diabatic spin−orbit constants of 7.7 and 18.1 cm^{-1} for the couplings to $(\alpha)^3A_1$ and $(\beta)^3A_1$, respectively, using coordinates obtained by doubling the displacement between the calculated CCSD minima for $(\alpha)^3A_1$ and $(\beta)^3A_1$, and this ratio is used for the transition moments in the simulations.

4.3. Singlet-to-Triplet Absorption. To model the singlet-to-triplet absorption spectra, two simulations were performed. The first one is restricted to just the totally symmetric modes whereas the second includes the two b_1 modes as well. It is a good approximation to ignore the effects of the antisymmetric modes for the simulation of low-resolution absorption spectrum as their effects are small in the Franck−Condon region.

4.3.1. Effects of the Totally Symmetric Modes. Shown in Figure 8 is the calculated low-resolution spectrum (obtained using a Gaussian spectral window of resolution 600 cm^{-1} and harmonic-oscillator Franck−Condon factors to describe the effects of the a_1 modes not explicitly included in the simulation), and this is compared to the observed solution spectrum[22] and low-energy electron-loss spectra. Detailed comparisons of the band shapes are not possible, as the observed spectra arise because of processes different from the intramolecular spin−orbit-facilitated absorption that is modeled, with in particular the intensity of the solution spectrum coming through intermolecular coupling with added triplet oxygen. However, the calculated spectrum is in qualitative agreement with the experimental data.

The intensity distribution in the low-frequency (3.6−3.9 eV) region of the spectrum shown in Figure 8 is adjusted to match that observed in the high-resolution gas-phase absorption spectrum.[23] At low frequency are observed two weak lines, the first at 29 652 cm^{-1} (3.67 eV) with the spacing to the next line being +115 cm^{-1}. However, the next-highest-frequency observed lines are in a band of eight lines ranging from +1999 to +2052 cm^{-1}, the two most intense lines being at +2049 and +2052 cm^{-1}. This rather unusual spacing has led to the speculation that more than one triplet state is involved.[23] Our interpretation is that the first two lines arise from the transition to the origin of $(\alpha)^3A_1$, in resonance with a level associated with the $^3A'$ boatlike structure, whereas the intensity at +2000 cm^{-1} arises from the transition to the quasi-origin of $(\beta)^3A_1$, with this line being split into a number of lines due to the background densities of states arising from the $(\alpha)^3A_1$ and $^3A'$ wells. The key vibrational levels are indicated on the insert in Figure 4 in which the marked energy levels are, in energy order, the $(\alpha)^3A_1$ origin, this plus one quantum of mode 8a, the $(\beta)^3A_1$ quasi-origin, and two higher levels involving ν_{8a} that lie above the transition state between $(\alpha)^3A_1$ and $(\beta)^3A_1$. Interference between the second and third levels results in a weakening of the second band, calculated to be at +1486 cm^{-1}, and an intensification of the third, at +2055 cm^{-1}. The model predicts the occurrence of a variety of other transitions in the +600 to +1400 cm^{-1} region, but all of these are attributed less intensity than the $(\alpha)^3A_1$ origin (although their combined intensity is significant, as can be seen from the calculated second peak at 3.8 eV in the low-resolution spectrum shown in Figure 8), whereas the $(\beta)^3A_1$ origin is an order of magnitude more intense. Using the assumption that the intermediary lines are individually too weak to have been observed in the high-resolution spectrum, this analysis interprets all of the main features of the observed spectrum. The parameters in the model on which the calculated intensity pattern depend most sensitively are the transition-moment ratio, which we have kept fixed at the calculated spin−orbit coupling ratio; the energy offset $\Delta E_{\alpha\beta}$; the displacements δ_{8a}; and, to a lesser extent, the electronic coupling $J_{\alpha\beta}$.

4.3.2. Effects of the Boat Distortion in the b_1 Modes. Finally, we performed expanded simulations in which the two primary b_1 modes, 16b and 11, were also included, thus allowing a complete simulation of the vibrational levels of the $^3A'$ hypersurface. Some significant changes to the absorption intensity pattern resulted. Most noticeably, a large number of low-lying vibrational levels associated with the additional well were produced. In all, the vibrational basis set for this simulation was truncated using 6, 6, 5, 8, 25, and 25 quanta in modes 6a, 1, 9a, 8a, 16b, and 11, respectively, truncating to ensure that all included levels contained no more that 25 quanta total; the dimension of the resulting Hamiltonian matrix was thus 106 919. The lowest calculated energy level, which, in terms of the crude-adiabatic basis functions comprises 17% $(\alpha)^3A_1$, 32% $(\beta)^3A_1$, and 51% $^3B_1$, is at an energy of −999 cm^{-1} relative to the origin of $(\alpha)^3A_1$, with three other intermediary levels predicted. Neither this energy gap nor the number of intermediary levels are robust features of the model, however, both being quite sensitive to the vibronic coupling and $\Delta E_{\alpha n}$ parameters. The fifth level had an interaction of strength 30 cm^{-1} with the $(\alpha)^3A_1$ origin, ca. half that required to produce the splitting of 115 cm^{-1} between the first two observed lines, but sufficiently large to indicate the plausibility of the suggested scenario. Above the $(\alpha)^3A_1$ origin, lines of similar intensity occur at +1077, +1080, +1368, and +1439 cm^{-1}, while the absorption to the $(\alpha)^3A_1$ origin plus one quantum of ν_{8a} is now split into three lines covering 1622−

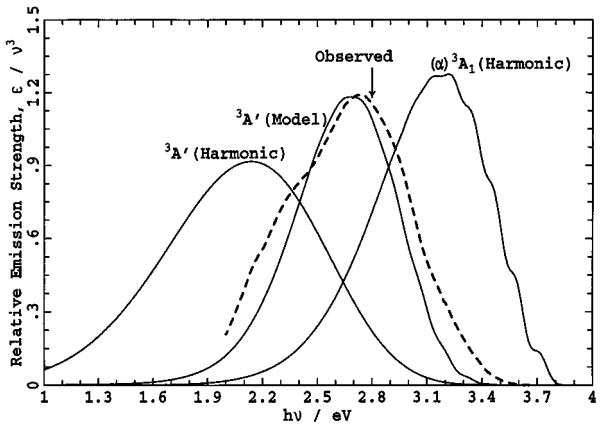

Figure 9. The observed[24] gas-phase phosphorescence spectrum of pyridine is compared to those obtained using the Harmonic and Condon approximations and the CCSD harmonic force field for the $(\alpha)^3A_1$ (C_{2v}) and $^3A'$ (boatlike) local minima, as well as that obtained from the full vibronic coupling model.

1654 cm^{-1} and is twice as intense as the origin. This intensity comes from a change in the nature of the interference with the $(\beta)^3A_1$ C_{2v} origin, which is only twice as intense again and split into seven lines covering 1857−1933 cm^{-1}.

Hence, we see that addition of the b_1 modes to the model has resulted in too much intensity being attributed to the region of the spectrum between the observed initial pair of lines and the clump at ca. +2000 cm^{-1}. It is, however, clear that small changes to the parameters can result in significant changes to the intensity pattern and the depth of the $^3A'$ well. These simulations, for which almost all of the parameters are taken from the results of CCSD or other calculations, thus only indicate the feasibility of the depicted scenario. A significant source of error in the model is the use of rectilinear normal coordinates to describe the large-angle out-of-plane boat distortion. Curvilinear coordinates would provide a much better description of the shape of the potential surface and would lead to less coupling with the totally symmetric modes. In particular, the depth for the boatlike $^3A'$ well from the model Hamiltonian is significantly deeper than the calculated antisymmetric-mode reorganization energies indicate (see Table 7), reflecting the inadequacy of our simple vibronic coupling expansion in rectilinear coordinates. Improved coordinates would lead to a shallower well and a higher $(\alpha)^3A_1$−$(\beta)^3A_1$ transition state (see Figure 6) and, hence, would significantly reduce the impact on the calculated spectra due to the inclusion of the b_1 modes in the simulations. Also, improved calculations of the vibrational structure could possibly be obtained through a direct Born−Oppenheimer analysis of the entire $^3A_1$ hypersurface. However, the occurrence of two conical intersections within the Franck−Condon region (see Figure 6) may prevent this.

4.4. Phosphorescence. The observed gas-phase phosphorescence spectrum of pyridine[24] is shown in Figure 9, along with various simulated spectra, while the observed and calculated vertical emission energies E_{VE} are shown in Table 17. The simulated spectra include two obtained using harmonic Condon analyses, which include all Duschinsky rotation effects, based on the calculated CCSD force fields for the $(\alpha)^3A_1$ (C_{2v}) and $^3A'$ (boatlike) minima, whereas that for $^3A'$ is far too broad. This is also reflected in the vertical emission energies, with Table 17 showing that all quality methods predict emission from $^3A'$ to be 0.5−0.9 eV lower in energy than is the observed phosphorescence, while the emission from $(\alpha)^3A_1$ is predicted 0.2−0.6 eV higher; the calculated ground-state reorganization energies (from Tables 8 and 17) also follow this pattern.

Either of two simple scenarios could explain these discrepancies. First, if the out-of-plane distortions of the $^3A'$ minimum are reduced to 75% of their calculated magnitudes, λ_G would be significantly reduced, and a good fit to the observed spectrum would be obtained. Second, if the vibronic coupling between $(\alpha)^3A_1$ and $^3B_1$ is increased so that the $(\alpha)^3A_1$ surface develops a shallow double minimum in mode 16b, then the emission from $(\alpha)^3A_1$ would be much broader, akin to the effect shown in Figure 7 for the fluorescence from $^1B_1$, and the observed spectrum thus could be reproduced. However, as both of these scenarios are inconsistent with the results of almost all of the computational methods, we suggest that neither is appropriate.

We have calculated the emission spectrum originating from the lowest energy level of the model $^3A'$ surface, treating all modes not explicitly included in the model Hamiltonian using harmonic-oscillator Franck−Condon factors without Duschinsky rotation, and the calculated spectrum is shown in Figure 9. It is in good agreement with the observed spectrum. However, this result must be taken cautiously, as the emitting level is constructed through a slowly convergent expansion in terms of undisplaced harmonic oscillators. Poor convergence of this expansion, or poor choice of the vibronic coupling constants, will result in a decrease in the effective out-of-plane displacement magnitude, surreptitiously eliminating the disagreement between theory and experiment. We estimate that the combined effect on λ_G of these shortcomings is 0.2 eV, only one-third of the calculated correction obtained using the computed excited-state wave function compared to Franck−Condon analysis at the $^3A'$ optimized geometry; hence, we believe that our approach does, in fact, reveal the true nature of the origin of the phosphorescence.

Other factors may also shift the calculated emission from $^3A'$ up by of order 0.2 eV. First, use of the BLYP or B3LYP force fields rather than that from CCSD decreases λ_G by this amount. More subtly, in our model we assumed that the transition moments to $(\alpha)^3A_1$ and $(\beta)^3A_1$ are coordinate-independent. To test this, we generated a revised model electronic Hamiltonian to which the $^1B_1$ state is added, coupled to $(\alpha)^3A_1$ and $(\beta)^3A_1$ using the CASSCF spin−orbit coupling constants. By diagonalizing this four-state electronic Hamiltonian, new Born−Oppenheimer energy and transition-moment surfaces were generated on the assumption of a coordinate-independent $S_0 \rightarrow {}^1B_1$ transition moment. The resulting transition moment, expressed relative to that at the CCSD $^3A'$ minimum, is shown in Figure 10 as a function of the relative displacement in the two key b_1 modes. As the boat structure is displaced back toward the ground-state structure, the transition moment increases nonlinearly as, at the ground-state geometry, the $^3B_1$, $(\alpha)^3A_1$, $(\beta)^3A_1$, and $^1B_1$ states are all much closer in energy. Inclusion of this transition-moment profile in the harmonic-oscillator spectrum also results in a shift of the band center up by 0.15 eV and preferentially intensifies the transitions near the band origin. Hence, it appears clear that the observed phosphorescence does indeed emerge from the nonplanar $^3A'$ well rather than the planar $(\alpha)^3A_1$ well. Through comparisons of the calculated and observed phosphorescence spectra, it appears likely that the model potentials do underestimate the energy of the $^3A'$ origin by ca. 0.1 eV.

5. Conclusions

Experimentally, a great deal of information is known about both the low-lying singlet and low-lying triplet states of pyridine. For the singlet states, detailed assignments are available, and our ab initio and density-functional calculations have been able

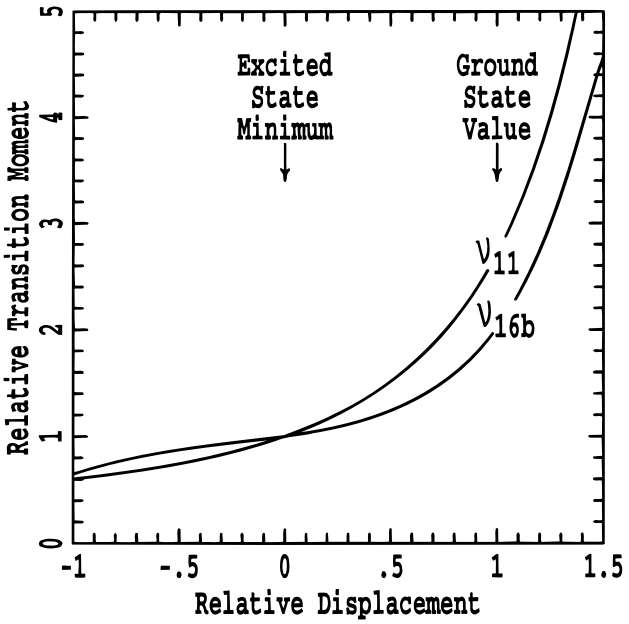

Figure 10. The phosphorescence transition moment, relative to its value at the $^3A'$ (boatlike) minimum, is shown as a function of the relative displacement in the b_1 modes ν_{16b} and ν_{11} from that configuration, evaluated by diagonalizing the model electronic Hamiltonian representing the coupled $^1B_1$, $^3B_1$, $(\alpha)^3A_1$, and $(\beta)^3A_1$ states.

to reproduce the key features of the vertical absorption energies, the geometry relaxation, and the vibrational motions. We have, however, identified a new feature, a low-lying conical intersection between the (n,π^*) $^1B_1$ (S_0) and $^1A_2$ (S_3) states, and we suggest that this should bring about experimentally measurable effects on energy flow through the singlet manifold.

For the triplet states, only tentative assignments had been suggested for the observed singlet-to-triplet absorption spectra, no assignment of the observed phosphorescence had been suggested, and the observed spin resonance in benzene crystal had been interpreted as coming from a state of 80% (π,π^*) and 20% (n,π^*) character. It was known that two low-lying triplet states, one $^3B_1$ and the other $^3A_1$, were implicated. We have shown that the lowest triplet Born−Oppenheimer surface, $^3A'$, is very complex and results from *three* strongly interacting crude-adiabatic surfaces, $^3A_1$, $(2)^3A_1$, and $^3B_1$. The two A_1 states interact through strong vibronic coupling in the high-frequency a_1 mode 8a, giving rise to breakdown of pseudo-parity pairing and thus localization of the single-electron excitations α ($a_2 \rightarrow a_2$) and β ($b_1 \rightarrow b_1$), forming two potential wells named $(\alpha)^3A_1$ and $(\beta)^3A_1$, respectively. Our model of the observed spectra indicates the presence of a small barrier (height ca. 0.2 eV) separating these wells, although the TD-B3LYP calculated barrier is quite tiny, and further, CASPT2 and EOM-CCSD predict that the electronic coupling between these diabatic wells is sufficient to remove the barrier altogether. These two states also are vibronically coupled to $^3B_1$, the strongest interaction involving $(\beta)^3A_1$ through vibration 16b. As a result, $(\alpha)^3A_1$ remains a local minimum of C_{2v} symmetry on the $^3A'$ potential-energy hypersurface, while the $(\beta)^3A_1$ and $^3B_1$ C_{2v} structures become transition states leading to a boatlike local-minimum structure of C_s symmetry that is slightly lower in energy than $(\alpha)^3A_1$. Estimates have been obtained for the geometry and energy of low-lying transition states and conical intersections on this surface. The calculated structure of the $^3A'$ minimum agrees well with that deduced from ESR spectroscopy,[26,27] as do the calculated atomic spin densities and the assignment of the state as 80% (π,π^*) and 20% (n,π^*) character (using Born−Oppenheimer rather than crude-adiabatic orbitals). In moving from the C_{2v} structures to this structure, minimal change in character is found for $(\beta)^3A_1$; from $(\alpha)^3A_1$, the energy must first rise until the $(\alpha)^3A_1-(\beta)^3A_1$ transition state is passed, and from $^3B_1$, the energy falls continuously as the $^3B_1-(\beta)^3A_1$ conical intersection is quickly passed by.

Our calculations indicate that intensity of the singlet-to-triplet high-resolution absorption spectrum and the phosphorescence spectrum is provided via spin−orbit coupling of the two $^3A_1$ states to $^1B_1$. The phosphorescence[24] is assigned to the lower boatlike $^3A'$ well, but the observed lowest-energy absorption line[23] is assigned to $(\alpha)^3A_1$, split through resonance with a vibrational level from the $^3A'$ well. The observed anomalous spacing of ca. 2000 cm^{-1} is attributed to a vertical transition to $(\beta)^3A_1$.

To complete these calculations, we introduced a new method by which vibronic coupling constants for states displaying strong vibronic coupling (strong enough to cause symmetry lowering of the lower state) can be determined by analyzing calculated low-symmetry optimized geometries. This technique can be applied to results obtained using any electronic structure technique, and we found that its application to EOM-CCSD data led to the evaluation of vibronic coupling constants of sufficient accuracy to assign complex spectra.

In analyzing the results of electronic-structure calculations on molecular excited states, it is most common (see, e.g., refs 36−39 and 61) to compare computed vertical excitation energies to experimental band maxima. We show that it is, in fact, necessary to obtain the actual experimental average absorption frequency as well as the zero-point correction energy, as these contributions are often larger than the errors typically associated with modern computational methods such as EOM-CCSD, CASPT2, and TD-DFT.

A key aspect of our analysis is the use of a large range of computational methods to study the excited states. The shapes of excited-state potential-energy surfaces are very sensitive to vibronic couplings and the locations of conical intersections, and hence small changes in calculated vertical excitation energies can produce marked changes in the depth, location, and vibration frequencies of excited-state minima. Overall, the best results were produced using the EOM-CCSD and CASPT2 methods, with the accuracy of the TD-DFT methods being slightly lower. However, CASPT2 is not well suited to geometry optimizations and frequency calculations, because of the lack of available derivative codes, and, as CASSCF often produces poor structures, the most reliable use of CASPT2 is to apply it to either EOM-CCSD or TD-DFT geometries. These results are similar to those we have already obtained for pyrazine;[55,62] however, significantly different results have been obtained for molecules such as water[63] and H_2[64] whose excited states involve either Rydberg and/or dissociative character.

Naively, methods such as CCSD and direct DFT would be thought to be poorly applicable to (π,π^*) excited states because of their inherent single-configuration nature (see Appendix A.4). However, we found that their use essential to the final analysis, as they provided properties directly for the interacting diabatic states. Our final simulations of the complex $^3A'$ manifold were obtained using the CCSD harmonic potential-energy surfaces for the $(\alpha)^3A_1$, $(\beta)^3A_1$, and $^3B_1$ states, modified only by a 10% change to the displacements δ_{8a}, with vibronic coupling constants fitted to reproduce the energy and geometry of the $^3A'$ minimum, CASSCF spin−orbit couplings, and three energy parameters whose values were chosen empirically to fit the

observed spectra, constrained to be with the range spanned by the CASPT2 and EOM-CCSD results.

Appendix: Electronic Structure Computational Methods

A.1. Methodological Implementations. All time-dependent density-functional[39,45−48,65] calculations (TD-B3LYP and TD-BLYP) were performed using TURBOMOLE[66] using the "M3" integration grid and the energy convergence criterion set to 10^{-10} au, with all derivatives evaluated numerically in internal coordinates using our own program. The direct DFT (B3LYP and BLYP) calculations (performed using the Gunnarsson−Lundqvist theorem[67]) and all CIS geometry optimizations and frequency calculations were performed with the aid of analytical derivatives using Gaussian 98.[68] The CCSD[42] and EOM-CCSD[44] calculations were performed using analytical first derivatives by ACES II.[69] CASSCF geometry optimizations were typically performed using DALTON,[70] but sometimes MOLCAS[71] or MOLPRO[72] (for conical intersections), and a suitably modified form of Gaussian 98[68] was used to evaluate spin−orbit coupling constants. CASSCF harmonic-frequency calculations were performed using the analytical derivatives available in the DALTON[70] package. Single-point energy calculations were performed at the CASPT2 level using the MOLCAS[71] package.

For most calculations we use the polarized double-ζ cc-pVDZ[73] basis set. Some significant single-point energies are also evaluated using the expanded triple-ζ cc-pVTZ[73] and diffuse-function-augmented aug-cc-pVDZ[74] basis sets. The effects are small, however, with the computed results usually improving slightly as the basis set is expanded. High-lying excited states, especially those with significant Rydberg character, are known to require extensive basis sets, but none of the transitions considered herein are affected. Also, standard density functionals are not appropriate for Rydberg states; although corrections can successfully be applied,[63,65] they are clearly not required.

A.2. CASSCF Active Space Design. An important feature of the CASSCF and CASPT2 methods is the need to choose an active space (n,m), where n is the number of electrons distributed among m orbitals. For single-point energy calculations at high-symmetry geometries, Roos et al.[8,36] have shown that certain high-lying orbitals are of particular importance, and their inclusion in differently selected active spaces for (n,π^*) and (π,π^*) states leads to more rapid convergence of the calculated energies toward the experimental values. These approaches are inappropriate at distorted geometries of low symmetry, however, and consequently, Becucci et al.[9] have used a smaller (8,7) active space to describe distortions of $^1B_1$. Nevertheless, the smallest active space that contains all of the valence π orbitals that could feasiblely produce continuous potential-energy surfaces for the low-lying excited states as a function of small displacements in arbitrary directions is (10,14). The nature of this active space is apparent from Figure 1 in which the SCF orbital energies of pyridine within the range of −0.55 to 0.4 au are shown. An a_1 orbital that lies outside of the energy range spanned by the valence π orbitals is included in the active space as the relative energy of this orbital is quite variable. Unfortunately, this (10,-14) active space is too large for the range of calculations we perform, and hence we adopt a smaller (8,11) active space, excluding the three b_2 orbitals. Hence, our active space can, at best, produce continuous potential-energy surfaces for the low-lying states only when they undergo a_1 or b_1 distortions, the scenario of greatest interest herein. Using this active space, the number of orbitals of irreducible representation a_1, b_1, a_2, and b_2 constrained to be doubly occupied are 10, 0, 0, and 7, respectively, while 5, 4, 2, and 0 orbitals, respectively, are active. Note from Table 3 that the results obtained from our CASPT2 calculations agree quite well with those of Lorentzon, Fülscher and Roos,[8] even though our active space is optimized for surface generation rather than for the prediction of the best-possible vertical excitation energies.

For calculations of spin−orbit coupling constants in C_1 symmetry, we employ a (10,7) active space in which only the two lowest-lying virtual (π^*) orbitals are included.

A.3. Discontinuity Problems with CASSCF-Based Methodologies. We selected the (8,11) active space for this study, as it is the smallest active space containing all of the valence π electrons that could conceivably produce continuous potential-energy surfaces as a function of b_1 normal modes such as ν_{16b}. However, we find that the CASSCF surface for $^3B_1$ is, in fact, discontinuous at C_{2v} geometries, and electronic symmetry breaking leads to a lowering of the total energy. This effect is quite common, and the calculated values of the discontinuity found for various CASSCF and CASPT2 surfaces are shown in Table 11. The value of the antisymmetric relaxation energies shown in Table 7 are obtained from the difference in energy of the optimized structure and that at the C_{2v} geometric minimum, in both cases using C_s electronic symmetry. One expects that the magnitude of the CASPT2 discontinuity will be less than the corresponding CASSCF one, but the energy change may be positive, indicating that the CASPT2 energy in broken electronic symmetry exceeds that in high electronic symmetry.

When CASSCF potential-energy surfaces are discontinuous, vibration frequencies obtained using analytical derivatives with enforced high electronic symmetry are ill-defined. Sometimes, absurd results are generated, and these quickly signal the presence of discontinuities; at other times, realistic values are reported, the interpretation of which can lead to incorrect conclusions.[55] An example of the later problem can be found in CASSCF(8,7) calculations[9] on pyridine $^1B_1$: as shown in Table 7, this active space leads to a discontinuous surface, the minimum of which has reduced symmetry, but all vibration frequencies calculated at the C_{2v} geometry are reported to be positive,[9] incorrectly suggesting that CASSCF predicts high symmetry. Note that, in Table 11, the magnitude of the CASSCF discontinuity appears smaller for the (8,7) active space than for the (8,11) one. This is because a second (intruder-state) discontinuity is present when (8,7) is used, and the two effects tend to cancel.

The proper way to treat the problem of discontinuities is either to expand the active space or state averaging until the discontinuities disappear or to subsequently resymmetrize using a generalized valence-bond type approach.

A.4. Overview of the Types of Methods Used. The computational methods used can be divided into three types: (1) those that are based on multi-configurational excited-state wave functions, (2) those that are based on single-configuration excited-state descriptions, and (3) those that perturb the ground-state electronic description. Each type has its intrinsic strengths and weaknesses, and we consider the results obtained by methods of each type in turn.

Multiconfigurational methods are, in principle, the ones most suited to excited states as they treat strongly interacting configurations properly in zeroth order; these include the CASSCF, CASPT2, and MRCI methods. From the calculated root-mean-square (RMS) deviation between computed and observed vertical excitation energies shown in Table 3, we see that the CASPT2 method does particularly well, with an RMS error of ca. 0.2 eV. Its disadvantages, however, include the

computational resources required, the lack of availability of analytical derivative implementations, slow convergence with improved levels of theory,[62] and discontinuity and topology problems associated with its reliance on a possibly poor zeroth-order CASSCF starting wave function (see ref 55 and Appendix A.3). An advantage of the CASSCF technique is that it is particularly well suited to the determination of conical intersections, spin−orbit couplings, vibronic couplings, etc.

The second class of methods, CCSD, CCSD(T), BLYP, and B3LYP, can (reliably) be performed only for the lowest triplet state of each point-group symmetry.[67] They employ spin-unrestricted techniques, setting the orbital occupation to match one of the single excitations depicted in Figure 1. Hence, the wave function or density used in the zeroth-order calculation involves only a single electronic configuration. In the CCSD and CCST(T) methods, other configurations are included but are treated differently than the primary configuration. Their predictions (see Table 3) have RMS errors of ca. 0.1 eV, and the small differences between the CCSD and CCSD(T) results indicates that the one-determinant approach is, in practice, quite acceptable in this application. Direct density-functional calculations are similar but contain no explicit inclusion of the effects of configurations other than the primary one. However, they do include electron correlation intrinsically, and hence do, to an unknown extent, implicitly include configurational mixing effects. The RMS error shown for B3LYP in Table 3 of 0.24 eV, but this increases for BLYP to 0.39 eV, as this method significantly underestimates the energy of $^3A_2$.

The third class of computation methods construct excited states based on zeroth-order calculations for the ground state; these include CIS, CNDO/S, EOM-CCSD, EOM-CCSD(T), TD-B3LYP, and TD-BLYP. All of these methods treat each possible single excitation equivalently; their weakness is, however, that the ground state is not necessarily a good starting point for the description of excited states. In particular, CIS makes no allowance for dynamic electron correlation and thus considerably overestimates the energies of the excited states (RMS error of 1.2 eV from Table 3). Such effects are properly included in EOM-CCSD, however, for which the RMS error falls to ca. 0.2 eV. Typically, the addition of triples corrections in EOM-CCSD(T) results in transition energies that are lower by ca. 0.3 eV and in better agreement with experiment (see Del Bene et al.[37]), but from the available data for pyridine, this correction appears slightly too large. The time-dependent density-functional method TD-B3LYP produce a RMS error of 0.38 eV, significantly poorer than the results obtained using direct B3LYP with all transition energies being predicted to be uniformly lowered. However, results obtained using TD-BLYP are rather poor (RMS error is 0.68 eV), this being due principally to significant underestimation of the energies of A_2 states.

Like EOM-CCSD, TD-B3LYP and TD-BLYP are formulated using approximate propagators to solve the time-dependent Schrödinger equation for excitation of the ground state. In this regard, these methods appear as approximations to full CCSD, B3LYP, and BLYP calculations, respectively, and the differences in the results can be attributed to the effects of the time-dependent propagator used. However, these approximations result in an improved treatment of strongly interacting single-electron excitations, and hence, it is not clear a priori which method is expected to give the best results; for related problems, we have found the situation to be quite variable.[62−64]

Acknowledgment. We gratefully acknowledge financial assistance from the Australian Research Council for the completion of this work.

Supporting Information Available: Provided in ASCII format are 71 calculated geometries (49 full optimization, 19 from one-dimensional scans along normal modes of imaginary frequency, 3 estimated by linear interpolation), as well as 44 sets of normal modes, with associated Duschinsky matrices and displacement projections; 44 pages, 86 kBytes. This material is available free of charge via the Internet at http://pubs.acs.org.

References and Notes

(1) Innes, K. K.; Ross, I. G.; Moomaw, W. R. *J. Mol. Spectrosc.* **1988**, *132*, 492.
(2) Chachisvilis, M.; Zewail, A. H. *J. Phys. Chem. A* **1999**, *103*, 7408.
(3) Innes, K. K.; Byrne, J. P.; Ross, I. G. *J. Mol. Spectrosc.* **1967**, *22*, 125.
(4) Dilella, D. P.; Stidham, H. D. *J. Raman Spectrosc.* **1980**, *9*, 90.
(5) Davidsson, Å. *Chem. Phys.* **1980**, *45*, 409.
(6) Stidham, H. D.; DiLella, D. P. *J. Raman Spectrosc.* **1980**, *9*, 247.
(7) Destexhe, A.; Dsmets, J.; Adamowicz, L.; Maes, G. *J. Phys. Chem.* **1994**, *98*, 1506.
(8) Lorentzon, L.; Fülscher, M. P.; Roos, B. O. *Theor. Chim. Acta* **1995**, *92*, 67.
(9) Becucci, M.; Lakin, N. M.; Pietraperzia, G.; Salvi, P. R.; Castellcui, E.; Kerstel, E. R. Th. *J. Chem. Phys.* **1997**, *107*, 10399.
(10) Martin, J. M. L.; Van Alsenoy, C. *J. Phys. Chem.* **1996**, *100*, 6973.
(11) Martoprawiro, M. A.; Bacskay, G. B. *Mol. Phys.* **1995**, *85*, 573.
(12) Mason, S. F. *J. Chem. Soc.* **1959**, 1240.
(13) Goodman, L. *J. Mol. Spectrosc.* **1961**, *6*, 109.
(14) Bolovinos, A.; Tsekeris, P.; Philis, J.; Phantos, E.; Andritsopoulos, G. *J. Mol. Spectrosc.* **1984**, *103*, 240.
(15) Yamazaki, I.; Baba, H. *J. Chem. Phys.* **1977**, *66*, 5826.
(16) Mochizuki, Y.; Kaya, K.; Ito, M. *J. Chem. Phys.* **1978**, *69*, 935.
(17) Yamazaki, I.; Sushida, K.; Baba, H. *J. Chem. Phys.* **1979**, *71*, 381.
(18) Yamazaki, I.; Murao, T.; Yoshihara, K.; Fujita, M.; Sushida, K.; Baba, H. *Chem. Phys. Lett.* **1982**, *92*, 421.
(19) Villa, E.; Amirav, A.; Lim, E. C. *J. Phys. Chem.* **1988**, *92*, 5393.
(20) Walker, I. C.; Palmer, M. H.; Hopkirk, A. *Chem. Phys.* **1989**, *141*, 365.
(21) Jesson, J. P.; Kroto, H. W.; Ramsay, D. A. *J. Chem. Phys.* **1972**, *56*, 6257.
(22) Evans, D. F. *J. Chem. Soc.* **1957**, 3885.
(23) Japar, S.; Ramsay, D. A. *J. Chem. Phys.* **1973**, *58*, 5832.
(24) Sushida, K.; Fujita, M.; Takemura, T.; Baba, H. *J. Chem. Phys.* **1983**, *78*, 588.
(25) Bos, F. C.; Buma, W. J.; Schmidt, H. *Chem. Phys. Lett.* **1985**, *117*, 203.
(26) Buma, W. J.; Groenen, E. J. J.; Schmidt, J. *Chem. Phys. Lett.* **1986**, *127*, 189.
(27) Buma, W. J.; Groenen, E. J. J.; Schmidt, J.; de Beer, R. *J. Chem. Phys.* **1989**, *91*, 6549.
(28) Selco, J. I.; Holt, P. L.; Weisman, R. B. *J. Chem. Phys.* **1983**, *79*, 3269.
(29) Doering, J. P.; Moore, J. H., Jr. *J. Chem. Phys.* **1972**, *56*, 2176.
(30) Chang, H. M.; Jaffé, H. H.; Masmanidis, C. A. *J. Phys. Chem.* **1975**, *79*, 1109.
(31) Kitao, O.; Nakatsuji, H. *J. Chem. Phys.* **1988**, *88*, 4913.
(32) Nagaoka, S. I.; Nagashima, U. *J. Phys. Chem.* **1990**, *94*, 4467.
(33) Buma, W. J.; Groenen, E. J. J.; van Hermert, M. C. *J. Am. Chem. Soc.* **1990**, *112*, 5447.
(34) Foresman, J. B.; Head-Gordon, M.; Pople, J. A.; Frisch, M. J. *J. Phys. Chem.* **1992**, *96*, 135.
(35) Hochstrasser, R. M.; Marzzacco, C. A. In *Molecular Luminesence*; Lim, E. C., Ed.; Benjamin: New York, 1969.
(36) Fülscher, M. P.; Andersson, K.; Roos, B. O. *J. Phys. Chem.* **1992**, *96*, 9204.
(37) Del Bene, J. E.; Watts, J. D.; Bartlett, R. J. *J. Chem. Phys.* **1997**, *106*, 6051.
(38) Nooijen, M.; Bartlett, R. J. *J. Chem. Phys.* **1997**, *106*, 6441.
(39) Bauernschmitt, R.; Ahlrichs, R. *Chem. Phys. Lett.* **1996**, *256*, 454.
(40) Hegarty, D.; Robb, M. A. *Mol. Phys.* **1979**, *38*, 1795.
(41) Andersson, K.; Malmqvist, P.-Å.; Roos, B. O. *J. Chem. Phys.* **1992**, *96*, 1218.
(42) Purvis, G. D., III; Bartlett, R. J. *J. Chem. Phys.* **1982**, *76*, 1910.
(43) Raghavachari, K.; Trucks, G. W.; Pople, J. A.; Head-Gordon, M. *Chem. Phys. Lett.* **1989**, *157*, 479.
(44) Stanton, J. F.; Bartlett, R. J. *J. Chem. Phys.* **1993**, *98*, 7029.
(45) Bauernschmitt, R.; Häser, M.; Treutler, O.; Ahlrichs, R. *Chem. Phys. Lett.* **1997**, *264*, 573.
(46) Casida, M. E.; Jamorski, C.; Casida, C. K.; Salahub, D. R. *J. Chem. Phys.* **1998**, *108*, 4439.

(47) Stratmann, R. E.; Scuseria, G. E.; Frisch, M. J. *J. Chem. Phys.* **1998**, *109*, 8218.
(48) van Gisbergen, S. J. A.; Kootstra, F.; Schipper, P. R. T.; Gritsenko, O. V.; Snijders, J. G.; Baerends, E. J. *Phys. Rev. A* **1998**, *57*, 2556.
(49) Becke, A. D. *J. Chem. Phys.* **1993**, *98*, 5648.
(50) Becke, A. D. *Phys. Rev. A* **1988**, *38*, 3098.
(51) Lee, C.; Yang, W.; Parr, R. G. *Phys. Rev. B* **1988**, *37*, 789.
(52) Del Bene, J.; Jaffe, H. H. *J. Chem. Phys.* **1968**, *48*, 1807, 4050.
(53) Coulson, C.; Richardson, G. S. *Philos. Soc.* **1940**, *36*, 193.
(54) Scott, A. P.; Radom, L. *J. Phys. Chem.* **1996**, *100*, 16502.
(55) Weber, P.; Reimers, J. R. *J. Phys. Chem. A* **1999**, *103*, 9830.
(56) Fischer, G. *Vibronic coupling: The interaction between the electronic and nuclear motions*; Academic Press: London, 1984.
(57) Wilson, E. B., Jr.; Decius, J. C.; Cross, P. C. *Molecular Vibrations*; McGraw-Hill: New York, 1955.
(58) Robey, M. J.; Ross, I. G.; Southwood-Jones, V. R.; Strickler, S. J. *Chem. Phys.* **1997**, *23*, 207.
(59) Chappell, P. J.; Fischer, G.; Reimers, J. R.; Ross, I. G. *J. Mol. Spectrosc.* **1981**, *87*, 316.
(60) Hochstrasser, R. M.; Marzzacco, C. *J. Chem. Phys.* **1968**, *49*, 971.
(61) Foresman, J. B.; Head-Gordon, M.; Pople, J. A.; Frisch, M. J. *J. Phys. Chem.* **1992**, *96*, 135.
(62) Weber, P.; Reimers, J. R. *J. Phys. Chem. A* **1999**, *103*, 9821.
(63) Cai, Z.-L.; Tozer, D. J.; Reimers, J. R. *J. Chem. Phys.* **2000**, in press.
(64) Cai, Z.-L.; Reimers, J. R. *J. Chem. Phys.* **2000**, *112*, 527.
(65) Tozer, D. J.; Amos, R. D.; Handy, N. C.; Roos, B. O.; Serrano-Andrés, L. *Mol. Phys.* **1999**, *97*, 859.
(66) Ahlrichs, R.; Bär, M.; Baron, H.-P.; Bauernschmitt, R.; Böcker, S.; Ehrig, M.; Eichkorn, K.; Elliot, S.; Haase, F.; Häser, M.; Horn, H.; Huber, C.; Huniar, U.; Kattannek, M.; Kölmel, C.; Kollwitz, M.; Ochsenfeld, C.; Öhm, H.; Schäfer, A.; Schneider, U.; Treutler, O.; von Arnim, M.; Weigend, F.; Weis, P.; Weiss, H. *TURBOMOLE*, version 4; Quantum Chemistry Group, University of Karlsruhe: Karlsruhe, Germany, 1997.
(67) Gunnarsson, O.; Lundqvist, B. I. *Phys. Rev. B* **1976**, *13*, 4274.
(68) Frisch, M. J.; Trucks, G. W.; Schlegel, H. B.; Scuseria, G. E.; Robb, M. A.; Cheeseman, J. R.; Zakrzewski, V. G.; Montgomery, J. A.; Stratmann, R. E.; Burant, J. C.; Dapprich, S.; Millam, J. M.; Daniels, A. D.; Kudin, K. N.; Strain, M. C.; Farkas, O.; Tomasi, J.; Barone, V.; Cossi, M.; Cammi, R.; Mennuci, B.; Pomelli, C.; Adamo, C.; Clifford, S.; Ochtersi, J.; Patterson, G. A.; Ayala, P. Y.; Cui, Q.; Morokuma, K.; Malick, D. K.; Rabuck, A. D.; Raghavachari, K.; Foresman, J. B.; Cioslowski, J.; Ortiz, J. V.; Stefanov, B. B.; Liu, G.; Liashenko, A.; Piskorz, P.; Komaromi, I.; Gomperts, R.; Martin, R. L.; Fox, D. J.; Keith, T.; Al-Laham, M. A.; Peng, C. Y.; Nanayakkara, A.; Gonzalez, G.; Challacombe, M.; Gill, P. M. W.; Johnson, B. G.; Wong, W. Chen.; Wong, M. W.; Andres, J. L.; Head-Gordon, M.; Replogle, E. S.; Pople, J. A. *Gaussian 98*, rev. A7; Gaussian Inc.: Pittsburgh, 1998.
(69) Stanton, J. F.; Gauss, J.; Watts, J. D.; Nooijen, M.; Oliphant, N.; Perera, S. A.; Szalay, P. G.; Lauderdale, W. J.; Gwaltney, S. R.; Beck, S.; Balková, A.; Bernholdt, D. E.; Baeck, K.-K.; Rozyczko, P.; Sekino, H.; Hober, C.; Bartlett, R. J. *ACES II*; Quantum Theory Project, University of Florida: Gainseville, FL, 1999.
(70) Helgaker, T.; Jensen, H. J. Aa.; Joergensen, P.; Olsen, J.; Ruud, K.; Aagren, H.; Andersen, T.; Bak, K. L.; Bakken, V.; Christiansen, O.; Dahle, P.; Dalskov, E. K.; Enevoldsen, T.; Fernandez, B.; Heiberg, H.; Hettema, H.; Jonsson, D.; Kirpekar, S.; Kobayashi, R.; Koch, H.; Mikkelsen, K. V.; Norman, P.; Packer, M. J.; Saue, T.; Taylor, P. R.; Vahtras, O. *DALTON*, release 1.0; University of Lund: Lund, Sweden, 1997.
(71) Andersson, K.; Blomberg, M. R. A.; Füscher, M. P.; Karlström, G.; Lindh, R.; Malmqvist, P.-Å.; Neogrády, P.; Olsen, J.; Roos, B. O.; Sadlej, A. J.; Seijo, L.; Serrano-Andrés, L.; Siegbahn, P. E. M.; Widmark, P.-O. *MOLCAS*, version 4; University of Lund: Lund, Sweden, 1997.
(72) Werner, H.-J.; Knowles, P. J.; Almlöf, J.; Amos, R. D.; Deegan, M. J. O.; Elbert, S. T.; Hampel, C.; Meyer, W.; Peterson, K.; Pitzer, R.; Stone, A. J.; Taylor, P. R.; Lindh, R.; Mura, M. E.; Thorsteinsson, T. *MOLPRO 97*; University of Birmingham: Birmingham, U.K., 1997.
(73) Dunning, T. H., Jr. *J. Chem. Phys.* **1989**, *90*, 1007.
(74) Dunning, T. H., Jr.; Harrison, R. J. *J. Chem. Phys.* **1992**, *96*, 6796.
(75) Sadlej, A. J. *Collect. Czech. Chem. Commun.* **1988**, *53*, 1995.